cmgh
CELLULAR AND MOLECULAR GASTROENTEROLOGY AND HEPATOLOGY

ORIGINAL RESEARCH

Microbial-Dependent Recruitment of Immature Myeloid Cells Promotes Intestinal Regeneration

Zhengyu Jiang,[1,2,*] Quin T. Waterbury,[1,2,3,*] Ermanno Malagola,[1,2] Na Fu,[1,2,4] Woosook Kim,[1,2] Yosuke Ochiai,[1,2] Feijing Wu,[1,2,5] Chandan Guha,[6,7] Carrie J. Shawber,[8] Kelley S. Yan,[1,9,10] and Timothy C. Wang[1,2]

[1]Division of Digestive and Liver Diseases Medicine, Irving Cancer Research Center, Department of Medicine, Columbia University Medical Center, New York, New York; [2]Herbert Irving Comprehensive Cancer Center, Columbia University Medical Center, New York, New York; [3]Institute of Human Nutrition, Columbia University Medical Center, New York, New York; [4]Department of Traditional and Western Medical Hepatology, Third Hospital of Hebei Medical University, Shijiazhuang, Hebei, China; [5]Department of Thyroid and Breast Surgery, The Second Affiliated Hospital of Fujian Medical University, Quanzhou, Fujian, China; [6]Department of Radiation Oncology, Montefiore Medical Center, Bronx, New York; [7]Department of Pathology, Albert Einstein College of Medicine, Bronx, New York; [8]Department of Obstetrics and Gynecology, Columbia University Irving Medical Center, New York, New York; [9]Columbia Center for Human Development, Columbia University, New York, NY, USA; and [10]Department of Genetics and Development, Columbia University Medical Center, New York, New York

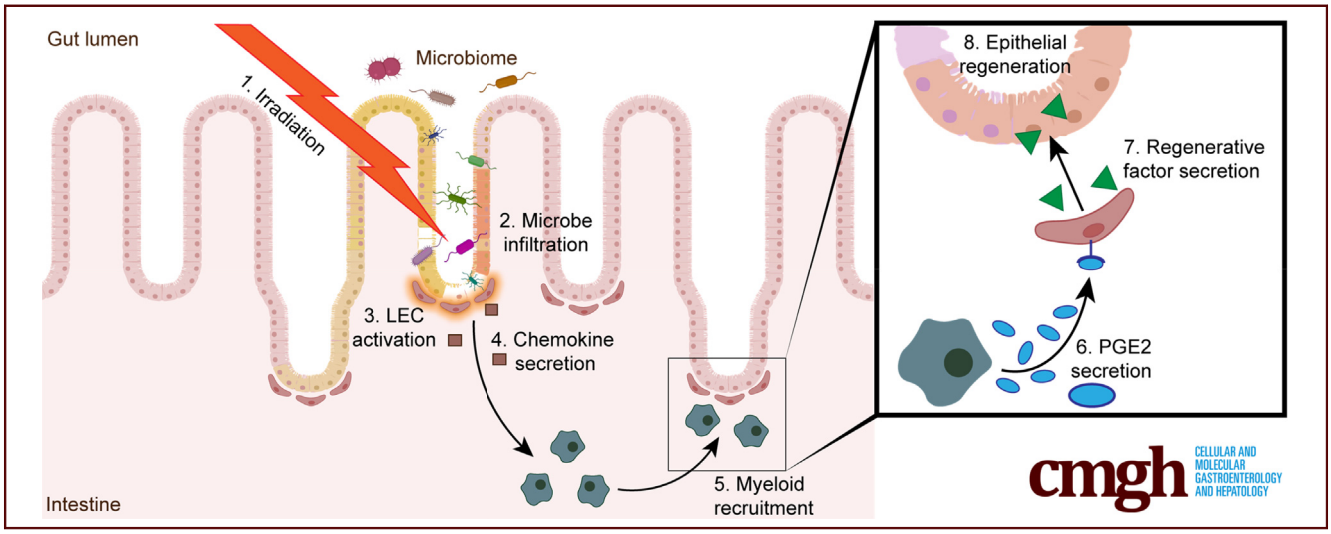

SUMMARY

This work presents a novel pathway of intestinal regeneration wherein infiltrating microbial signals promote the recruitment of granulocytic immature myeloid cells that activate proregenerative lymphatic cells. Ablation of the gut microbiome or immature myeloid cells reduces intestinal regeneration after irradiation injury.

BACKGROUND & AIMS: The intestinal epithelium functions both in nutrient absorption and as a barrier, separating the luminal contents from a network of vascular, fibroblastic, and immune cells underneath. After injury to the intestine, multiple cell populations cooperate to drive regeneration of the mucosal barrier, including lymphatic endothelial cells (LECs). A population of granulocytic immature myeloid cells (IMCs), marked by *Hdc*, participate in regeneration of multiple organs such as the colon and central nervous system, and their contribution to intestinal regeneration was investigated.

METHODS: By using male and female histidine decarboxylase (Hdc) green fluorescent reporter (GFP) mice, we investigated the role of Hdc^+ IMCs in intestinal regeneration after exposure to 12 Gy whole-body irradiation. The movement of IMCs was analyzed using flow cytometry and immunostaining. Ablation of Hdc^+ cells using the $Hdc^{CreERT2}$ tamoxifen-inducible recombinase Cre system, conditional knockout of Prostaglandin-endoperoxidase synthase 2 (*Ptgs2)* in Hdc^+ cells using Hdc^{Cre}; Ptgs2 floxed mice, and visualization of LECs using $Prox1^{tdTomato}$ mice also was performed. The role of microbial signals was investigated by knocking down mice gut microbiomes using antibiotic cocktail gavages.

RESULTS: We found that Hdc^+ IMCs infiltrate the injured intestine after irradiation injury and promote epithelial regeneration in part by modulating LEC activity. Hdc^+ IMCs express *Ptgs2* (encoding cyclooxygenase-2/COX-2), and enables them to produce prostaglandin E_2. Prostaglandin E_2 acts on the prostaglandin E_2 receptor 4 receptor (EP4) on LECs to promote lymphangiogenesis and induce the expression of proregenerative factors including R-spondin 3. Depletion of gut microbes leads to reduced intestinal regeneration by impaired recruitment of IMCs.

CONCLUSIONS: Altogether, our results unveil a critical role for IMCs in intestinal repair by modulating LEC activity and implicate gut microbes as mediators of intestinal regeneration. *(Cell Mol Gastroenterol Hepatol 2024;17:321–346; https://doi.org/10.1016/j.jcmgh.2023.10.007)*

Keywords: Myeloid; Endothelial Cell; PGE2; RSPO3; Microbiome.

Epithelial tissues such as the skin or intestine undergo constant stress and injury and must continuously regenerate to maintain proper barrier function. Compromise of the intestinal barrier leads to penetration of numerous microbial products from commensal bacteria, such as the endotoxin class lipopolysaccharides (LPS), which affects tissues locally and systemically. LPS exposure generally is considered harmful, so regeneration of the epithelium is tightly regulated to limit endotoxin exposure and maintain proper healing after injury without excessive growth.[1] In the intestine, epithelial regeneration relies on complex crosstalk between intestinal stem cells (ISCs), and surrounding niche cells, including endothelial cells, fibroblasts, and immune cells.[2–4] These niche cells produce several signals, including R-spondins, wingless-related integration site factors (Wnts), and epidermal growth factor (EGF) family ligands, that are essential for ISC maintenance and epithelial regeneration.[5–8]

One population of niche cells, lymphatic endothelial cells (LECs), have been shown to be an essential source of R-spondin 3 (RSPO3) in the intestine.[9,10] RSPO3 is the major ligand for the leucine rich repeat containing G protein coupled receptors 4 and 5 (LGR4/5)4/5 receptors on ISCs and progenitor cells and is necessary for proper regeneration after injury.[11] LECs exist in a network in the intestine that consists of a central lacteal located in the center of the villus, which connects to precollectors in the submucosa.[12] Precollector LECs surround the crypt base and associate with ISCs to regulate their activity.[10] This LEC population expands in the intestine after whole-body irradiation (WB-IR), and conditional knockout of the *Rspo3* gene in LECs hinders intestinal regeneration, highlighting the importance of LEC-derived RSPO3 in regenerating the intestine.[13,14] Lymphatics also expand in the bone after WB-IR and participate in bone regeneration.[15] Although the expansion of LECs and increased RSPO3 production are necessary for intestinal regeneration, it is unclear how LECs are activated and RSPO3 secretion is induced in response to intestinal injury. In addition to secreting niche factors, LECs are important mediators of inflammatory signaling by regulating the trafficking of immune cells from lymphoid organs to inflamed tissues. LECs are known to secrete several chemokines that modulate lymphocyte and dendritic cell migration during inflammation, such as CC motif chemokine ligand 21 (CCL21), CCL27, C-X-C motif chemokine ligand 12 (CXCL12), and CXCL14.[16–19] Although the role of LECs in immune regulation has been well studied in adaptive immunity,[20] how LECs regulate innate immune cells is less understood.

Myeloid cells, a type of innate immune cells, have been shown to play essential roles in intestinal homeostasis and regeneration.[21–23] During injury, lymphocyte antigen 6 family member C1 positive ($Ly6C^+$) monocytes accumulate rapidly in the intestine and integrate signals coming from gut microbes to the injured epithelium through Toll-like receptor (TLR) signaling.[24,25] Infiltrating monocytes are a vital source of Wnts that promote survival of $Lgr5^+$ cells during injury and epithelial repair.[3] Myeloid-derived Wnt signaling also plays an important role in regulating LEC proliferation in the dermal epithelium.[26] Myeloid cells also can regulate lymphatic cell angiogenesis through the production of vascular endothelial growth factor (VEGF)-A and VEGF-C.[27,28] In addition to Wnt and Vegf signaling, myeloid cells in the intestine also express *Ptgs2* (the gene encoding the cyclooxygenase-2 [COX-2] enzyme), which catalyzes the rate-limiting step in producing prostaglandin E_2 (PGE2).[29,30] PGE2 is a bioactive lipid that mediates inflammatory signals through several different types of receptors, including the E-type prostanoid receptors (EP).[31] PGE2 has been known to protect mice against IR injury–induced death since the 1980s.[32] Specifically, pretreating mice with PGE2 protects epithelial cells from IR-induced apoptosis by inhibiting Bcl-2-associated X protein (Bax) signaling.[33] Moreover, PGE2 also is able to promote intestinal epithelium repair by expanding the pool of regenerative progenitor cells through prostaglandin E_2 receptor 4 (EP4)-receptor signaling.[29,34,35] Notably, in breast tissue, PGE2 is a known activator of LEC lymphangiogenesis through the EP4 receptor,[36] but its role in regulating intestinal LECs is unknown.

A certain subset of immature myeloid cells (IMCs) expresses histidine decarboxylase (encoded by the gene *Hdc*).[37,38] Histidine decarboxylase $(Hdc)^+$ IMCs are primarily granulocytic, marked by $CD11b^+$ $Ly6G^+$, with a smaller subset being monocytic and $Ly6C^+$. During homeostasis, these cells comprise $\geq$80% of IMCs in the bone marrow and rarely are found in the circulation or peripheral tissues.[39] In addition to maintaining the bone marrow hematopoietic stem cell niche through histamine production, this IMC population is mobilized rapidly from the bone marrow to

***Authors share co-first authorship.**

Abbreviations used in this paper: **BrdU, bromodeoxyuridine; cDNA, complementary DNA; COX-2, cyclooxygenase-2; CreERT2, Cre recombinase - estrogen receptor T2; CXCL, chemokine (C-X-C motif) ligand; dmPGE2, 16,16 dimethylprostaglandin E_2; DTA, diptheria toxin subunit A; EGF, epidermal growth factor; EP4, prostaglandin E_2 receptor 4; EP4i, prostaglandin E_2 receptor 4 inhibitor; GFP, green fluorescent protein; HBSS, Hank's balanced salt solution; Hdc, histidine decarboxylase; HDLEC, human dermal lymphatic endothelial cell; IMC, immature myeloid cell; ISC, intestinal stem cell; LEC, lymphatic endothelial cell; LPS, lipopolysaccharide; LYVE1, lymphatic vessel endothelial hyaluronan receptor 1; $Ly6C^+$, lymphocyte antigen 6 family member C1; PBS, phosphate-buffered saline; PCR, polymerase chain reaction; Ptgs2, prostaglandin-endoperoxidase synthase 2; PGE2, prostaglandin E_2; qPCR, quantitative polymerase chain reaction; RSPO3, R-spondin 3; TLR, Toll-like receptor; VEGF, vascular endothelial growth factor; WB-IR, whole-body irradiation; Wnt, wingless-related integration site.**

Most current article

2352-345X
https://doi.org/10.1016/j.jcmgh.2023.10.007

damaged tissues in response to inflammatory conditions such as acute colitis, cancer, or LPS endotoxemia.[37,39,40]

Here, we studied the role of Hdc$^+$ IMCs in intestinal regeneration after IR injury. We found that after damage to the intestinal barrier, LECs are exposed to microbial-derived signals, which trigger their up-regulation of the chemokine *Cxcl1*. This in turn recruits Hdc$^+$ IMCs near intestinal LECs in a CXCR2-dependent manner. Within the intestine, Hdc$^+$ IMCs support mucosal regeneration by secreting PGE2, which activates the LECs through EP4 and promotes their up-regulation of proregenerative factors including *Rspo3*, *Ccl21a*, and *Wnt2a*. Using transgenic mouse models, we show that Hdc$^+$ IMCs are essential for mediating the response to microbial signals and orchestrating LECs' role in intestinal regeneration.

Results

Hdc$^+$ IMCs Are Recruited to the Damaged Intestine After Irradiation Injury

We previously have shown that Hdc$^+$ IMCs are mobilized from the bone marrow to the colon during *dextran* sodium sulfate–induced colitis and promote regeneration.[39] To test if Hdc$^+$ IMCs are involved in intestinal regeneration, we used a model of 12-Gy WB-IR, which induces acute damage to the intestinal epithelial stem and progenitor zone cells.[41] To track the movement of Hdc$^+$ IMCs, we took advantage of our previously generated Hdc-green fluorescent protein reporter (Hdc^{GFP}) mice, which fluorescently label the majority of CD11b$^+$ Ly6G$^+$ granulocytic IMCs.[38] Immunofluorescent visualization of the jejunum, and flow cytometry analyses of the jejunum and ileum, revealed that Hdc^{GFP+} cells are virtually absent from the small intestine of unirradiated mice, but infiltrate the tissue 3 days after 12-Gy WB-IR exposure (Figure 1*A*–*C*). Within 10 days after IR, when regeneration is mostly finished,[42] Hdc^{GFP+} cells were absent in the intestine. Importantly, immunophenotypic analysis of Hdc^{GFP+} cells in the intestine after irradiation confirmed that these cells are CD45$^+$ immune cells, and further analysis showed that approximately 95% are CD11b$^+$ Ly6G$^+$ granulocytic IMCs, with the remaining 5% consisting of CD11b$^+$ Ly6C+ monocytic IMCs (Figure 1*D*). *Hdc* also is expressed by other cell types such as basophils and mast cells,[43] however, we found that 0% of Hdc^{GFP+} cells in the intestine after irradiation were mast cells or basophils (Figure 1*D*). This finding aligns with our previously published data that mast cells and basophils are not marked in our Hdc^{GFP} mice, likely because of their expression of *Hdc* being lower than IMCs.[38]

Hdc$^+$ IMCs Are Indispensable for Intestinal Regeneration After IR

Because the gut-homing kinetics of Hdc$^+$ IMCs after WB-IR aligns with the temporal dynamics of intestinal regeneration, we hypothesized that these IMCs may be important for intestinal regeneration after IR. To test this hypothesis, we selectively ablated Hdc$^+$ cells in vivo using a tamoxifen-inducible diptheria toxin A mouse model (Hdc^{CreERT2}; R26^{DTA}).[37] After Cre induction via a tamoxifen-containing diet, Hdc^{CreERT2}; R26^{DTA} mice showed an up to 10-fold reduction in IMCs infiltrating the intestine 3 days post-IR, relative to wild-type controls (Hdc^{CreERT2}; R26^{WT}), confirming the cell depletion in this model (Figure 2*A*–*C*). We found no difference in the number of mast cells or basophils in the intestines of Hdc^{CreERT2}; R26^{DTA} after irradiation compared with controls (Figure 2*D*–*E*). Ablation of Hdc$^+$ cells in the setting of IR reduced intestinal regeneration, as evidenced by reduced villus length, epithelial cell proliferation, and fewer regenerating crypts in the jejunum of Hdc^{CreERT2}; R26^{DTA} mice relative to controls (Figure 2*F*–*I*). This impairment of intestinal regeneration was associated with decreased survival (Figure 2*J*). To confirm the role of Hdc$^+$ IMCs in intestinal regeneration, we performed adoptive transfer of CD11b$^+$; Hdc^{GFP+} or Hdc^{GFP-} bone marrow cells from nonirradiated Hdc^{GFP} mice into irradiated Hdc^{CreERT}; R26^{DTA} mice. Mice receiving Hdc^{GFP+} cells had significantly more IMCs accumulated in the intestine 6 days after IR and adoptive transfer, confirming that the transferred cells can home to the intestine (Figure 2*K*–*L*). Transfer of Hdc^{GFP+}, but not Hdc^{GFP-}, cells increased intestinal regeneration, suggesting that Hdc$^+$ IMCs contribute to intestinal regeneration more than their Hdc$^-$ counterparts (Figure 2*M*–*O*). Together, these results suggest that Hdc$^+$ IMCs are indispensable for intestinal regeneration after IR injury.

Hdc$^+$ IMCs Promote Epithelial Regeneration via Production of PGE2

Myeloid cells in the intestine are known to be sources of PGE2,[29,44] which has been shown to promote intestinal epithelial regeneration.[34,35] We previously reported that Hdc$^+$ IMCs express *Ptgs2*, encoding COX-2, a key enzyme responsible for PGE2 production.[40] Interestingly, we found that intestinally recruited Hdc$^+$ IMCs in irradiated mice significantly up-regulate *Ptgs2* expression compared with those found in the bone marrow of healthy mice (Figure 3*A*). However, Hdc$^+$ IMCs sorted from the bone marrow of irradiated mice do not up-regulate *Ptgs2*, suggesting that there may be specific signals in the intestine that promote this up-regulation. Sorted Hdc$^+$ IMCs from the intestine of irradiated mice express *Ptgs2* significantly more than their Hdc$^-$ counterparts, as previously reported (Figure 3*B*).[40] Finally, we performed immunostaining for COX-2 in the intestines of irradiated Hdc^{GFP} mice and found that a subset of Hdc$^+$ IMCs that infiltrate the intestine are positive for COX-2 (Figure 3*C*). Together, these data suggests that recruited Hdc$^+$ IMCs supply PGE2 to the regenerating intestine.

To study the role of Hdc$^+$ IMC-derived PGE2, we selectively abrogated Prostaglandin-endoperoxidase synthase 2 (*Ptgs2)* expression in Hdc$^+$ cells using Hdc^{Cre}; Ptgs2$^{fl/fl}$ mice.[45] After WB-IR exposure, overall *Ptgs2* expression increases within whole-jejunum tissue, but ablation of Hdc$^+$ cells or conditional knockout of *Ptgs2* in Hdc$^+$ cells significantly reduced this increase, indicating that infiltrating Hdc$^+$ IMCs are a major source of *Ptgs2* expression in the regenerating intestine (Figure 3*D*). Similarly, ablation of Hdc$^+$ cells or conditional knockout of *Ptgs2* in Hdc$^+$ cells significantly lowered the amount of COX-2$^+$ area in the jejunum via immunostaining (Figure 3*E* and *F*). These data suggests that during regeneration, infiltrating IMCs are a major source of

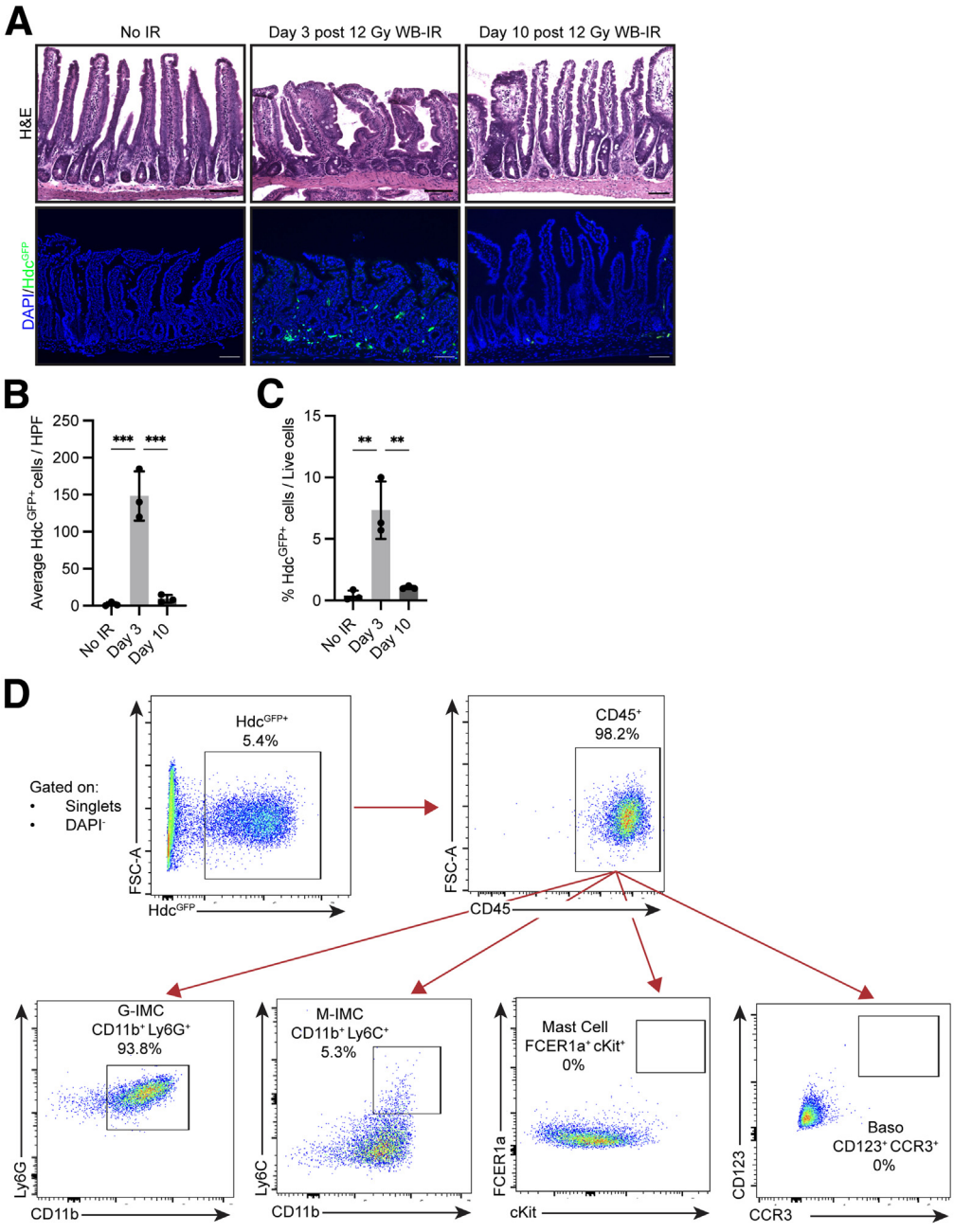

Figure 1. Hdc^{+} IMCs infiltrate the intestine after IR. (*A*) Representative 100× images of H&E staining (*top*) and immunofluorescence (*bottom*) from the proximal jejunum of Hdc^{GFP} mice that were unirradiated, or mice 3 and 10 days after 12-Gy WB-IR. (*B*) Bar plot showing quantification of GFP+ cells of images in panel *A*. n = 3. (*C*) Bar plot showing quantification of flow cytometric analysis of Hdc^{GFP+} cells isolated from the jejunum and ileum of unirradiated Hdc^{GFP} mice or mice 3 and 10 days after 12-Gy WB-IR. n = 3. (*D*) Representative FACS plots of 4′,6-diamidino-2-phenylindole (DAPI)$^{-}$ cells isolated from the jejunum and ileum of Hdc^{GFP} mice 3 days after 12-Gy WB-IR. *Scale bars*: 50 μm. Bar graph data are means ± SEM. (*B* and *C*) Statistical analysis was performed using an ordinary 1-way analysis of variance with multiple comparisons with each group. $^{**}P < .005$, $^{***}P < .0005$. Baso, basophil; FSC-A, forward scatter area; G-IMC, granulocytic IMC; HPF, high-power field; M-IMC, monocytic IMC.

COX-2. In line with this, after 12-Gy WB-IR challenge, Hdc^{Cre}; Ptgs2$^{fl/fl}$ mice showed significantly fewer proliferating bromodeoxyuridine-positive (BrdU^{+}) cells per crypt, reduced villus length, and fewer regenerating crypts in the jejunum compared with Hdc^{Cre} controls, mirroring what we observed in the setting of Hdc^{+} cell ablation (Figure 4*A*–*E*). Together, these results suggest that the regenerative capabilities of Hdc^{+} IMCs can be attributed, at least in part, to their expression of *Ptgs2* and secretion of PGE2.

PGE2 Promotes Epithelial Cell Expansion via the EP4 Receptor

PGE2 has been reported previously to promote intestinal regeneration by acting directly on epithelial cells through the EP4 receptor.[34,35] We confirmed these findings by treating intestinal organoids with the stable PGE2 analog 16,16 dimethylprostaglandin E_2 (dmPGE2) in vitro. Organoids treated with dmPGE2 showed increased diameter but not number, suggesting PGE2 may act as a growth factor for epithelial cells, consistent with previous literature.[29,35] The effects of dmPGE2 on organoids was reversed by adding a selective inhibitor for the prostaglandin receptor EP4 (EP4i) (Figure 4*F*–*H*).

Given the importance of IMC-derived PGE2 in intestinal epithelial regeneration after IR, we tested the effects of dmPGE2 in vivo on mice challenged with 12-Gy WB-IR. To distinguish from the reported function of dmPGE2 in protecting epithelial cells against IR-induced apoptosis, we

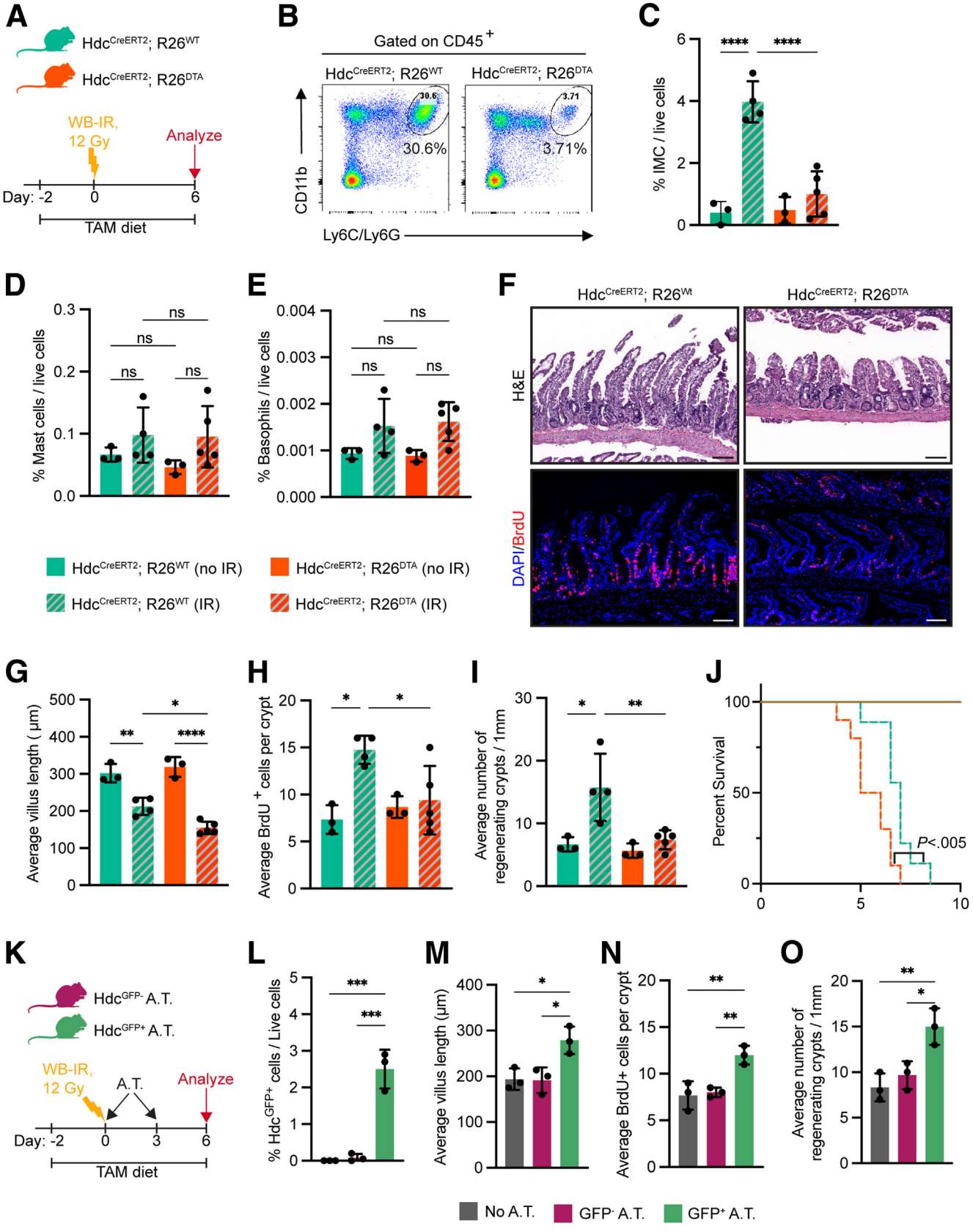
A
Hdc^CreERT2; R26^WT
Hdc^CreERT2; R26^DTA
WB-IR, 12 Gy
Analyze
Day: -2
0
6
TAM diet
B
Gated on CD45+
Hdc^CreERT2; R26^WT
Hdc^CreERT2; R26^DTA
30.6%
3.71%
CD11b
Ly6C/Ly6G
C
% IMC / live cells
****
****
D
% Mast cells / live cells
ns
E
% Basophils / live cells
ns
F
Hdc^CreERT2; R26^Wt
Hdc^CreERT2; R26^DTA
H&E
DAPI/BrdU
Hdc^CreERT2; R26^WT (no IR)
Hdc^CreERT2; R26^DTA (no IR)
Hdc^CreERT2; R26^WT (IR)
Hdc^CreERT2; R26^DTA (IR)
G
Average villus length (µm)
H
Average BrdU+ cells per crypt
I
Average number of regenerating crypts / 1mm
J
Percent Survival
P<.005
K
Hdc^GFP- A.T.
Hdc^GFP+ A.T.
WB-IR, 12 Gy
A.T.
Analyze
Day: -2
0
3
6
TAM diet
L
% Hdc^GFP+ cells / Live cells
M
Average villus length (µm)
N
Average BrdU+ cells per crypt
O
Average number of regenerating crypts / 1mm
No A.T.
GFP- A.T.
GFP+ A.T.

began treatment 2 days after IR, when apoptosis of epithelial cells already has occurred.[33,41] Five days after irradiation, dmPGE2-treated mice had increased BrdU$^+$ cells per crypt, villus length, and regenerating crypts compared with vehicle-treated mice, but these effects could be abrogated by pretreatment with EP4i (Figure 5*A*–*E*). Intriguingly, unirradiated mice that received dmPGE2 also showed an increased number of BrdU$^+$ cells per crypt, but no difference in villus length or regenerating crypt number, suggesting that the promitogenic activity of PGE2 is independent of tissue damage (Figure 5*F*–*I*). Altogether, these data indicate that IMC-derived PGE2 promotes intestinal regeneration, at least in part, by regulating epithelial proliferation through EP4 signaling.

Hdc$^+$ IMCs Activate LECs via a PGE2/EP4 Axis

Intestinal LECs are resistant to IR-induced apoptosis and expand during regeneration,[13,46] where they serve as an essential source of proregenerative niche factors such as RSPO3, Wnt2a, and Ccl21a.[9,10,14] Given that LEC expansion is most pronounced 3 days after IR, coinciding with the timing of intestinal infiltration of IMCs, we sought to investigate if there could be crosstalk between these cell types. To simultaneously track these cell populations, we crossed our Hdc^{GFP} mice with the Prox1^{tdTomato} allele, which labels LECs.[47] Three days after exposing these mice to 12- Gy WB-IR, Hdc$^+$ IMCs were found to localize within 20 μm of LECs in the jejunum, suggesting these cells may interact during intestinal regeneration (Figure 6*A* and *B*).

A population of RSPO3-secreting LECs in the intestine can be marked as CD31$^+$ CD90.2$^+$.[9] As previously published, this population of LECs expands 3 days after irradiation (Figure 6*C*). We further confirmed this population to be LECs by sorting them from the jejunum and ileum of healthy mice using fluorescence-activated cell sorter (FACS), and then analyzing their expression of *Lyve1*, *Pdpn*, *Prox1*, and *Vegfr3*, which distinguishes them from sorted blood endothelial cells (CD31$^+$ CD90.2$^-$) (Figure 6*D*).[48] Ablation of Hdc$^+$ cells during WB-IR in Hdc^{CreERT2}; R26^{DTA} mice diminished LEC expansion in the jejunum and ileum compared with controls (Figure 6*E*). Adoptive transfer of Hdc^{GFP+} IMCs (but not Hdc^{GFP-} IMCs) partially rescued this reduction, suggesting that Hdc$^+$ IMCs can regulate the expansion of LECs after irradiation (Figure 6*F*). Because our data indicate that Hdc$^+$ IMC-derived PGE2 is important for regeneration, we hypothesized that the reduction of LECs in the absence of IMCs may be owing to the lack of IMC-derived PGE2. In support of this hypothesis, PGE2 previously was described to induce lymphangiogenesis of LECs in vitro through the EP4 receptor.[36] We also found that intestinal LECs isolated via FACS primarily express *Ptger4*, the gene encoding the EP4 receptor (Figure 6*G*).

To determine if Hdc$^+$ IMC-derived PGE2 is important for LEC activity during regeneration, we returned to the Hdc^{Cre}; Ptgs2$^{fl/fl}$ mice. After WB-IR, Hdc^{Cre}; Ptgs2$^{fl/fl}$ mice had diminished lymphatic vessel endothelial hyaluronan receptor 1 (LYVE1+) area near the intestinal crypts in the jejunum compared with Hdc^{Cre} controls via immunostaining, and a smaller percentage of LECs via FACS analysis (Figure 7*A*–*C*). FACS-isolated LECs from the jejunum and ileum of Hdc^{Cre}; Ptgs2$^{fl/fl}$ mice after WB-IR also had reduced expression of the activation marker *Icam1*, and the proregenerative genes *Rspo3*, *Ccl21a*, and *Wnt2a* compared with controls (Figure 7*D*). Together, these data indicate that Hdc$^+$ IMC-derived PGE2 is important for activating LECs after IR injury.

Given the importance of Hdc$^+$ IMC-derived PGE2 on LECs during intestinal regeneration, we then asked if the observed increase in intestinal regeneration in irradiated mice treated with dmPGE2 could be owing to increased LEC activity. Mice that received dmPGE2 after 12-Gy WB-IR had an increased LEC percentage as well as lymphatic expansion near the small intestine crypt bases in the jejunum compared with controls, as shown by LYVE1 immunostaining and FACS analysis, and this effect was blocked by EP4i pretreatment (Figure 7*E*–*G*). FACS-isolated intestinal LECs from mice treated with dmPGE2 showed a higher gene expression of activation and proregenerative factors (Figure 7*H*).

Figure 2. (***See previous page***). **Hdc$^+$ IMCs are indispensable for intestinal regeneration.** (*A*) Experimental scheme of Hdc+ cell ablation experiment. (*B*) Representative FACS plot of 4′,6-diamidino-2-phenylindole (DAPI)$^-$, CD45$^+$, cells isolated from the jejunum and ileum of Hdc^{CreERT2} mice 3 days after 12-Gy WB-IR. (*C*) Bar plot showing quantification of panel *B*. n = 3, 4, or 5. (*D*) Bar plot showing quantification of FACS analysis of the percentage of mast cells out of live cells from the jejunum and ileum of mice from panel *A*. n = 3, 4, or 5. (*E*) Bar plot showing quantification of FACS analysis of the percentage of basophils of live cells from the jejunum and ileum of mice from panel *A*. n = 3, 4, or 5. (*F*) Representative 100× images of H&E (*top*) and BrdU (*bottom*) staining from the proximal jejunum of mice from panel *A*. (*G*) Bar plot showing quantification of the average villus length from panel *F*. n = 3, 4, or 5. (*H*) Bar plot showing quantification of BrdU staining from panel *F*. n = 3, 4, or 5. (*I*) Bar plot showing quantification of the average number of regenerating crypts per 1 mm from panel *F*. n = 3, 4, or 5. (*J*) Survival curve of mice from panel *D*. Hdc^{CreERT2}; R26^{DTA} no IR median, >10 days. Hdc^{CreERT2} with IR median, 7 days. Hdc^{CreERT2}; R26^{DTA} with IR median, 5.75 days. n = 5 (Hdc^{CreERT2}; R26^{DTA} no IR) or 10 (Hdc^{CreERT2} with IR and Hdc^{CreERT2}; R26^{DTA} with IR). (*K*) Experimental scheme of adoptive transfer study. (*L*) Bar plot showing quantification of FACS analysis of the percentage of Hdc^{GFP+} cells out of live (4′,6-diamidino-2-phenylindole [DAPI]-) cells from the jejunum and ileum of mice from panel *K*. n = 3. (*M*) Bar plot showing quantification of the average villus length of mice from panel *K*. n = 3. (*N*) Bar plot showing quantification of BrdU staining of mice from panel *K*. n = 3. (*O*) Bar plot showing quantification of the average number of regenerating crypts per 1 mm of mice from panel *K*. n = 3. *Scale bars*: 50 μm. Bar graph data are means ± SEM. Statistical analysis was performed using an (*C*–*E*, *G*–*I*, and *L*–*O*) ordinary 1-way analysis of variance with multiple comparisons with each group, or a (*J*) Kaplan–Meier simple survival analysis. *$P < .05$, **$P < .005$, ***$P < .0005$, ****$P < .00005$. A.T., adoptive transfer; TAM, tamoxifen.

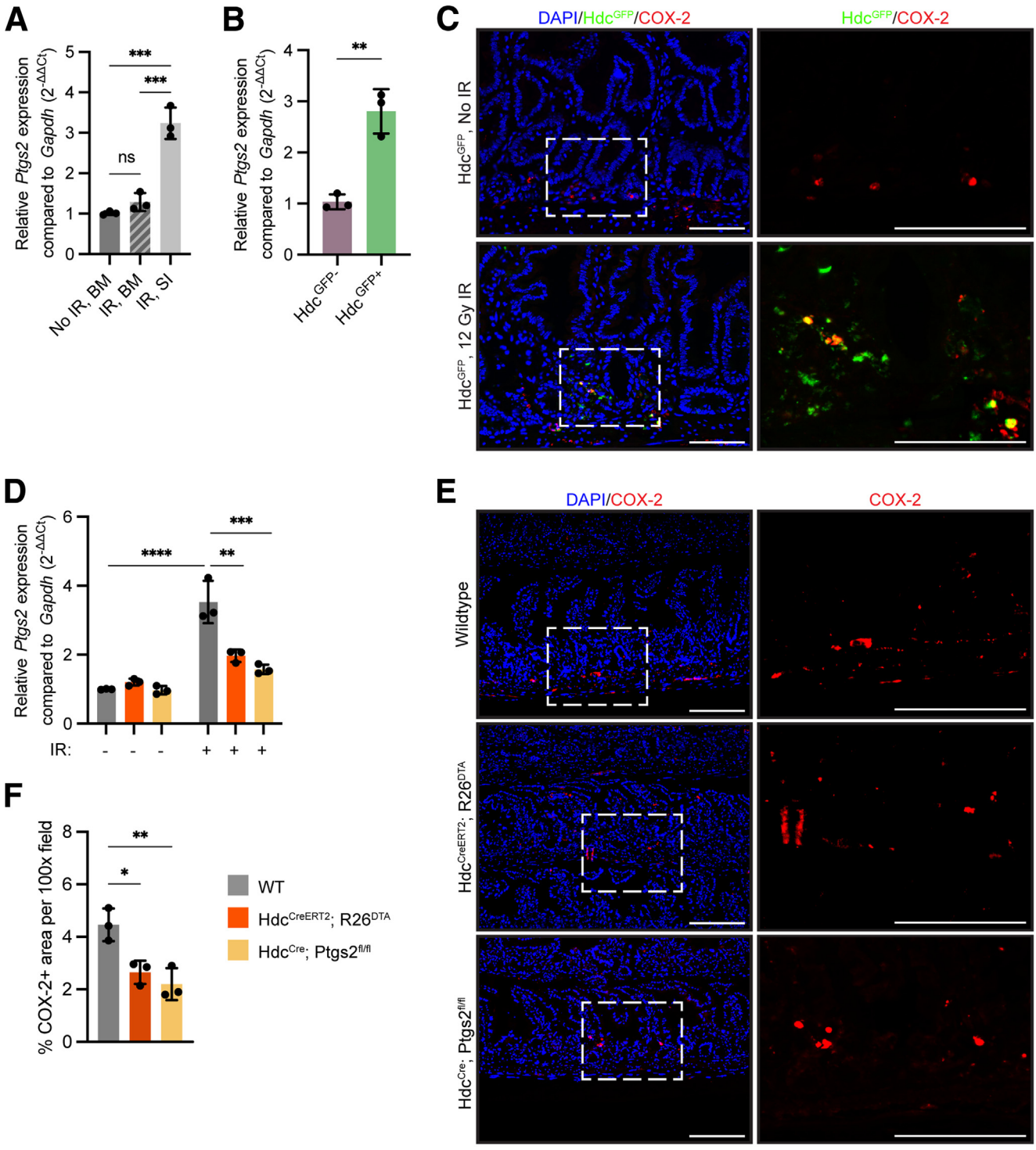

Figure 3. Hdc^{+} IMCs are a major source of intestinal COX-2 during regeneration. (*A*) Real time qPCR analysis of sorted Hdc^{+} IMCs from the bone marrow (BM) of unirradiated mice (No IR), or the BM, or jejunum and ileum of mice 3 days after 12-Gy WB-IR (IR). n = 3. (*B*) Real-time qPCR analysis of sorted CD45^{+} Hdc^{-} or CD45^{+} Hdc^{+} cells from the jejunum and ileum of mice 3 days after 12-Gy WB-IR. n = 3. (*C*) Representative 100× image of the proximal jejunum of unirradiated Hdc^{GFP} mice, or Hdc^{GFP} mice 3 days after 12-Gy WB-IR. (*D*) Real-time qPCR for *Ptgs2* from whole jejunum tissue of wild-type (WT), Hdc^{CreERT2}; R26^{DTA}, or Hdc^{Cre}; Ptgs2$^{fl/fl}$ mice either with no irradiation or 3 days after receiving 12-Gy WB-IR. n = 3. (*E*) Representative 100× images of COX-2 staining from the proximal jejunum of mice 3 days after 12-Gy WB-IR. (*F*) Bar plot showing quantification of the average COX-2–positive area per 100× field from images in panel *E*. n = 3. *Scale bars*: 50 μm. Bar graph data are means ± SEM. Statistical analysis was performed using an (*A*, *D*, and *F*) ordinary 1-way analysis of variance with multiple comparisons with each group, or a (*B*) 2-sided Student *t* test. *$P < .05$, **$P < .005$, ***$P < .0005$, ****$P < .00005$. DAPI, 4′,6-diamidino-2-phenylindole.

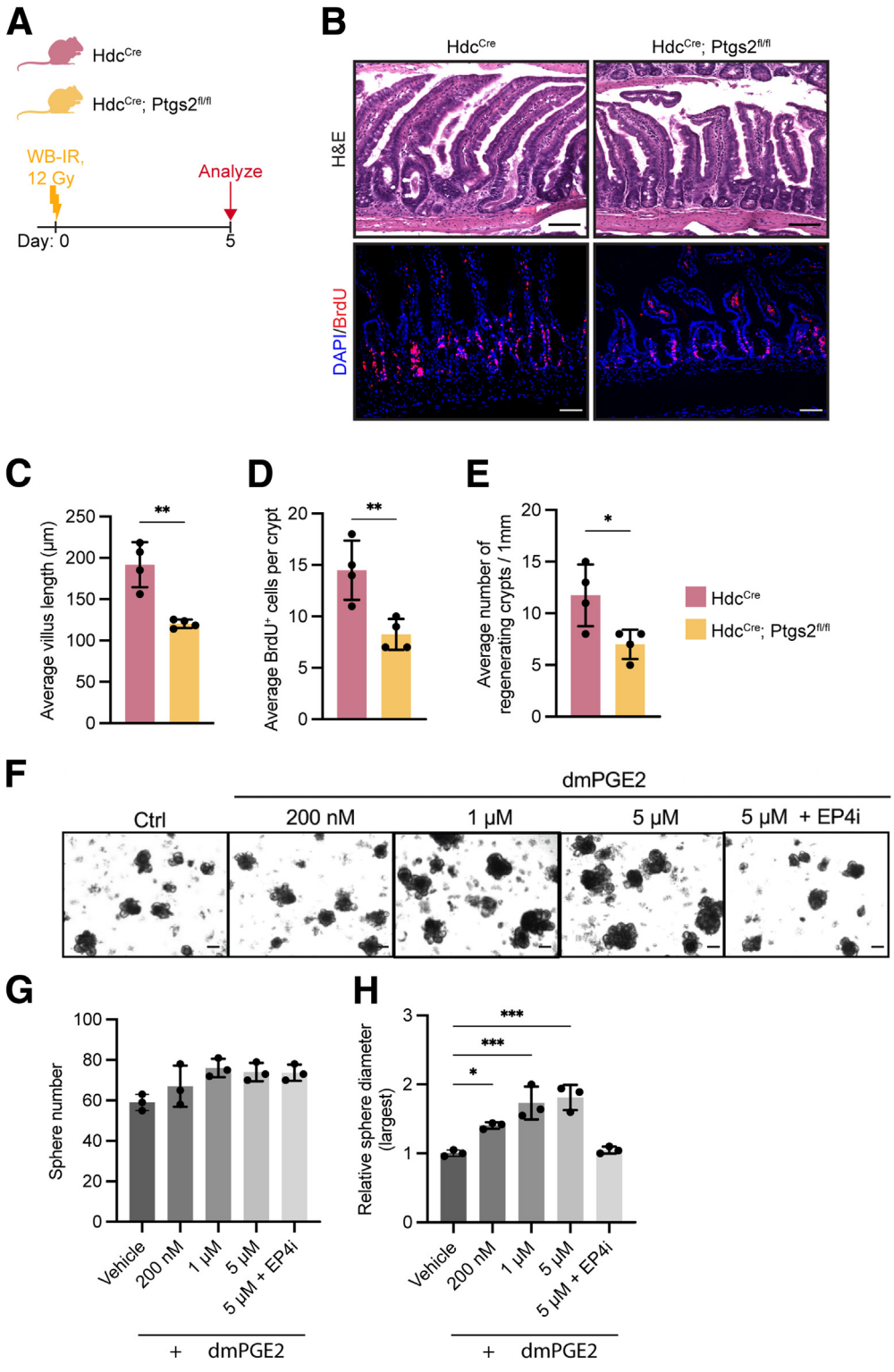

Figure 4. PGE2 from Hdc$^+$ IMCs promotes intestinal regeneration. (*A*) Experimental scheme of conditional *Ptgs2* knockout irradiation experiment. (*B*) Representative 100× images of H&E staining (*top*) and BrdU immunostaining (*bottom*) from the proximal jejunum of mice from panel *A*. (*C*) Bar plot showing quantification of the average villus length from panel *B*. n = 4. (*D*) Bar plot showing quantification of BrdU staining from panel *B*. n = 4. (*E*) Bar plot showing quantification of the average number of regenerating crypts per 1 mm from panel *B*. n = 3. (*F*) Representative 200× images of intestinal organoids in culture treated with various concentrations of dmPGE2 with or without EP4i. (*G*) Bar plot showing quantification of the average sphere number in panel *F*. n = 3. (*H*) Bar plot showing quantification of the average sphere size in panel *F*. n = 3. *Scale bars*: 50 μm. Bar graph data are means ± SEM. Statistical analysis was performed using a (*C*, *D*, and *E*) 2-sided Student *t* test or an (*G* and *H*) ordinary 1-way analysis of variance with multiple comparisons with each group. $^*P < .05$, $^{**}P < .005$, $^{***}P < .0005$. Ctrl, control. DAPI, 4′,6-diamidino-2-phenylindole.

To further investigate the direct effects of PGE2 on LECs, we used human dermal lymphatic endothelial cells (HDLECs), an in vitro model of LECs.[49] We performed bulk RNA sequencing on HDLECs treated with dmPGE2 or vehicle, and found that analysis of the pathways that are upregulated by dmPGE2 treatment revealed genes involved in endothelial cell adhesion, wound healing, and angiogenesis (Figure 8*A*). To confirm if PGE2 can induce lymphangiogenesis of HDLECs, we performed an in vitro endothelial cell bead sprouting assay.[50] HDLECs sprouted when treated with dmPGE2, but this was inhibited by EP4i treatment (Figure 8*B* and *C*). In addition, dmPGE2-treated HDLECs had a higher expression of activation and regenerative factors, and RSPO3 secretion, compared with cells treated with a

vehicle, but this effect could be diminished by co-treating the cells with EP4i (Figure 8*D* and *E*). These results indicate that PGE2 promotes LEC activation, sprouting, and expression of proregenerative factors through the EP4 receptor in vitro.

Taken together, these data indicate that PGE2 from infiltrating Hdc^{+} IMCs, besides acting directly upon the epithelium, also exerts effects on LECs via the EP4 receptor to promote activation, lymphangiogenesis, and expression of proregenerative factors.

Hdc^{+} IMCs Are Recruited to the Damaged Intestine via CXCR2 and CXCR4 Signaling

To better understand the connection between intestinal damage, Hdc^{+} IMCs, and LECs, we then investigated how Hdc^{+} IMCs initially are recruited to the damaged tissue. To this aim, we performed the RT^{2} Profiler polymerase chain reaction (PCR) (Qiagen) array for chemokine receptors on Hdc^{GFP+} cells isolated from the jejunum and ileum of Hdc^{GFP} mice 3 days after 12-Gy WB-IR. Results showed that these cells express high levels of the chemokine-receptor genes *Cxcr2* and *Cxcr4*, consistent with previous literature on granulocytic IMCs (Figure 9*A*).[51] LECs are known to secrete CXCL1 and CXCL12, ligands for CXCR2 and CXCR4, respectively, thus these chemokine receptors likely play a role in the recruitment of IMCs near intestinal LECs.[19,52] To determine if CXCR2 and CXCR4 signaling are important for Hdc^{+} IMC recruitment to the damaged intestine, we treated Hdc^{GFP} mice with a CXCR2 or CXCR4 inhibitor before and after exposure to IR (Figure 9*B*). Inhibition of CXCR2 or CXCR4 was sufficient to significantly reduce the number of Hdc^{+} cells infiltrating the intestine via histologic and FACS analysis of GFP^{+} cells, suggesting that these receptors are important for trafficking IMCs to the regenerating intestine (Figure 9*C*–*E*). In addition, we found that mice treated with a CXCR2 or CXCR4 inhibitor had reduced expansion of LECs in the jejunum and ileum 3 days after IR compared with controls, as measured by LYVE1 staining and flow cytometry (Figure 9*C*, *F*, and *G*). Inhibitor-treated mice also showed reduced regeneration in the jejunum 5 days after IR, as shown by reduced villus length, a lower number of BrdU^{+} cells per crypt, and fewer regenerating crypts in the jejunum compared with controls (Figure 9*H*–*K*).

The Microbiome Modulates Hdc^{+} IMC Recruitment and LEC Expansion

Next, we asked how CXCR2 and CXCR4 signaling could be initiated during intestinal injury. During intestinal barrier disruption, commensal microbes that reside in the lumen breach the barrier and contact the epithelium and underlying mesenchyme, initiating a variety of different responses from the niche.[53,54] LPS is a major component of the cell walls of gram-negative bacteria, and mediate intestinal inflammatory responses.[55] Previous studies have reported that LECs express the LPS receptor TLR4,[56] and exposing lymph node LECs to LPS causes them to secrete CXCL1.[52] We validated these findings in vitro by exposing HDLECs to LPS and found that these cells significantly up-regulate *CXCL1* and *CXCL8* (encoding interleukin 8, the human-specific CXCR2 ligand) compared to vehicle-treated controls (Figure 10*A*). In addition, LPS-stimulated HDLECs actively promoted migration of sorted Hdc^{+} IMCs in a co-culture migration assay, but this migration could be abrogated using a CXCR2 inhibitor or the mitogen-activated protein kinase kinase 1/2 (MEK1/2) antagonist U0126, which has been shown to inhibit CXCR2 signaling (Figure 10*B* and *C*).[57] We therefore hypothesized that LPS exposure from barrier disruption could serve as a trigger for Hdc^{+} IMC recruitment via LECs into the intestine through a CXCL1/CXCR2 axis. In support of this, we found that FACS-sorted intestinal LECs up-regulate their expression of *Cxcl1* compared with controls 3 days after WB-IR (Figure 10*D*).

To investigate if microbial signals can induce recruitment of IMCs in vivo, we used an endotoxemia model in which LPS was injected into unirradiated Hdc^{GFP} mice, which has been shown to mimic the entrance of microbes into the circulation during intestinal barrier disruption (Figure 10*E*).[58] After 3 days of LPS exposure, LECs from the jejunum and ileum of mice significantly up-regulated *Cxcl1* compared with controls, and this was associated with more Hdc^{+} IMCs infiltrating the jejunum mucosa (Figure 10*F*–*I*). These data suggest that LPS signaling can act upon intestinal LECs to trigger recruitment of Hdc^{+} IMCs, and this recruitment can occur independently of barrier damage.

Next, to test if gut microbes are necessary for recruiting IMCs after WB-IR, we gavaged Hdc^{GFP} mice twice daily with an antibiotic cocktail to deplete the intestinal microbiome, as previously reported.[59] Four days of antibiotic cocktail treatment significantly reduced the number of fecal bacteria compared with controls (Figure 11*A*). Three days after exposure to WB-IR (Figure 11*B*), antibiotic-treated mice had significantly fewer Hdc^{GFP+} cells infiltrating the jejunum and ileum (Figure 11*C*–*E*). Addition of LPS to the water of the antibiotic-treated mice after IR rescued the recruitment of Hdc^{GFP+} cells into the intestine, highlighting the importance of microbial signals in this recruitment pathway. FACS-sorted LECs from the jejunum and ileum of antibiotic-treated mice showed reduced expression of *Cxcl1*, which was rescued in mice supplied with LPS water (Figure 11*F*). Antibiotic-treated mice also had reduced expansion of LECs in the jejunum 3 days after IR, as measured by LYVE1 staining and flow cytometry, but this was rescued by LPS water (Figure 11*G* and *H*). Five days after WB-IR (Figure 12*A*), mice treated with antibiotics had significantly reduced villus length, number of BrdU^{+} cells per crypt, and regenerating crypts in the jejunum compared with controls, but these were all at least partially rescued by the addition of LPS to their drinking water (Figure 12*B*–*E*). These results suggest that signals coming from gut microbes activate LECs to promote IMC recruitment and initiate intestinal repair after epithelial barrier disruption. Together, these data suggest that microbial signals are a crucial trigger for LEC expression of *Cxcl1* and consequent recruitment of IMCs.

Discussion

The mammalian intestine has co-evolved with the gut microbiome and has developed mechanisms of interactions

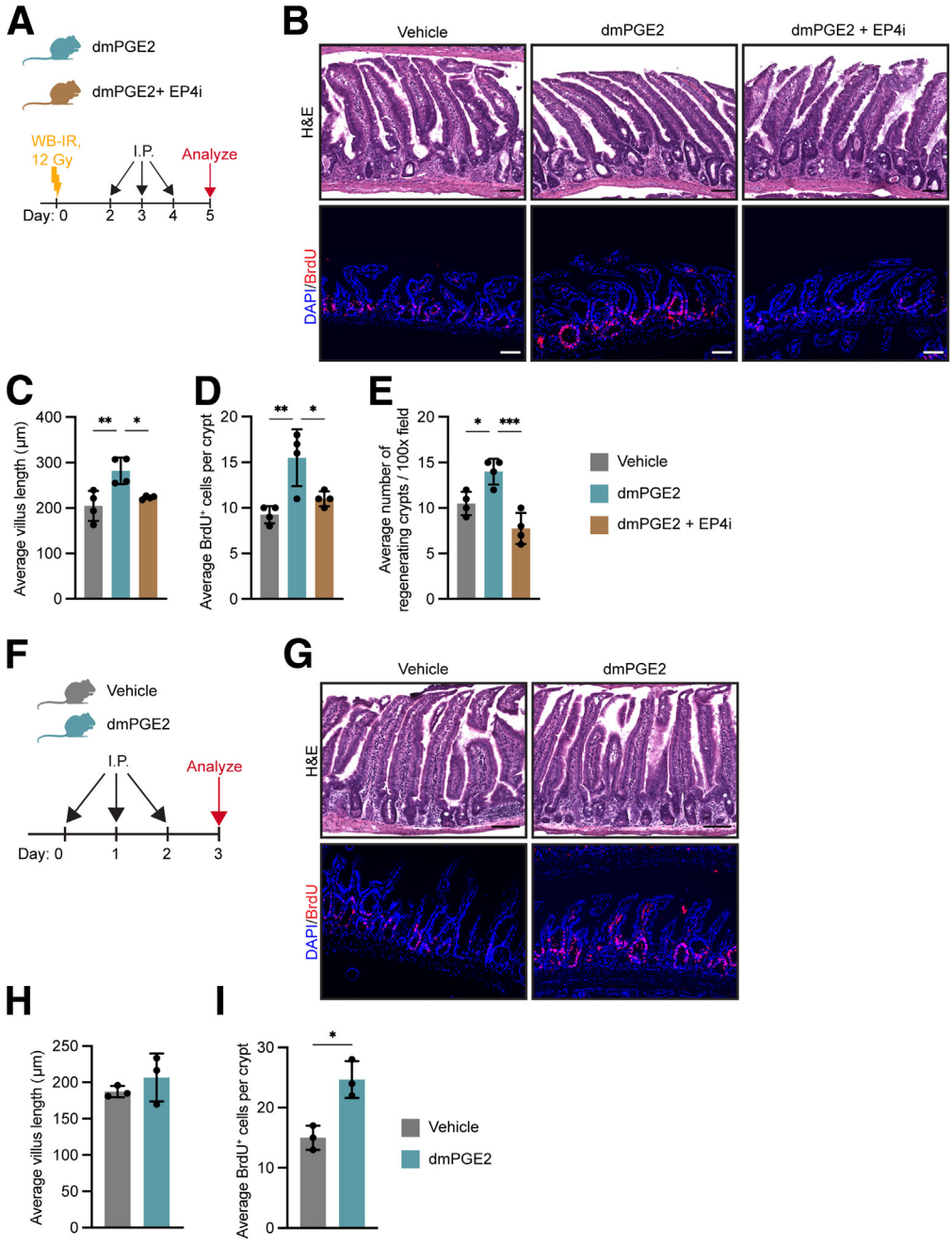

Figure 5. PGE2 promotes intestinal epithelial regeneration. (*A*) Experimental scheme of dmPGE2 treatment after irradiation experiment. (*B*) Representative 100× images of H&E staining (*top*) and BrdU immunostaining (*bottom*) from the proximal jejunum of mice from panel *A*. (*C*) Bar plot showing quantification of the average villus length from panel *B*. n = 4. (*D*) Bar plot showing quantification of BrdU staining from panel *B*. n = 4. (*E*) Bar plot showing quantification of the average number of regenerating crypts per 1 mm from panel *B*. n = 4. (*F*) Experimental scheme of dmPGE2 treatment experiment on healthy mice. (*G*) Representative 100× images of H&E (*top*) and BrdU (*bottom*) staining from the proximal jejunum of mice from panel *F*. (*H*) Bar plot showing quantification of the average villus length of images in panel *G*. n = 3. (*I*) Bar plot showing quantification of BrdU staining from panel *G*. n = 3. *Scale bars*: 50 μm. Bar graph data are means ± SEM. Statistical analysis was performed using an (*C*, *D*, and *E*) ordinary 1-way ANOVA with multiple comparisons with each group or a (*J* and *K*) 2-sided Student *t* test. **P* < .05, ***P* < .005, ****P* < .0005. IP, intraperitoneal injection of vehicle, dmPGE2, or dmPGE2 with EP4i pretreatment. DAPI, 4′,6-diamidino-2-phenylindole.

with these microbes to modulate host metabolism, immunity, and physiology. Breaches of the intestinal barrier cause disruptions to the balance of normal microbial interactions, requiring a response from the host to restore homeostasis. Lymphatic endothelial cells have been shown to be central to the intestinal regeneration program because they expand

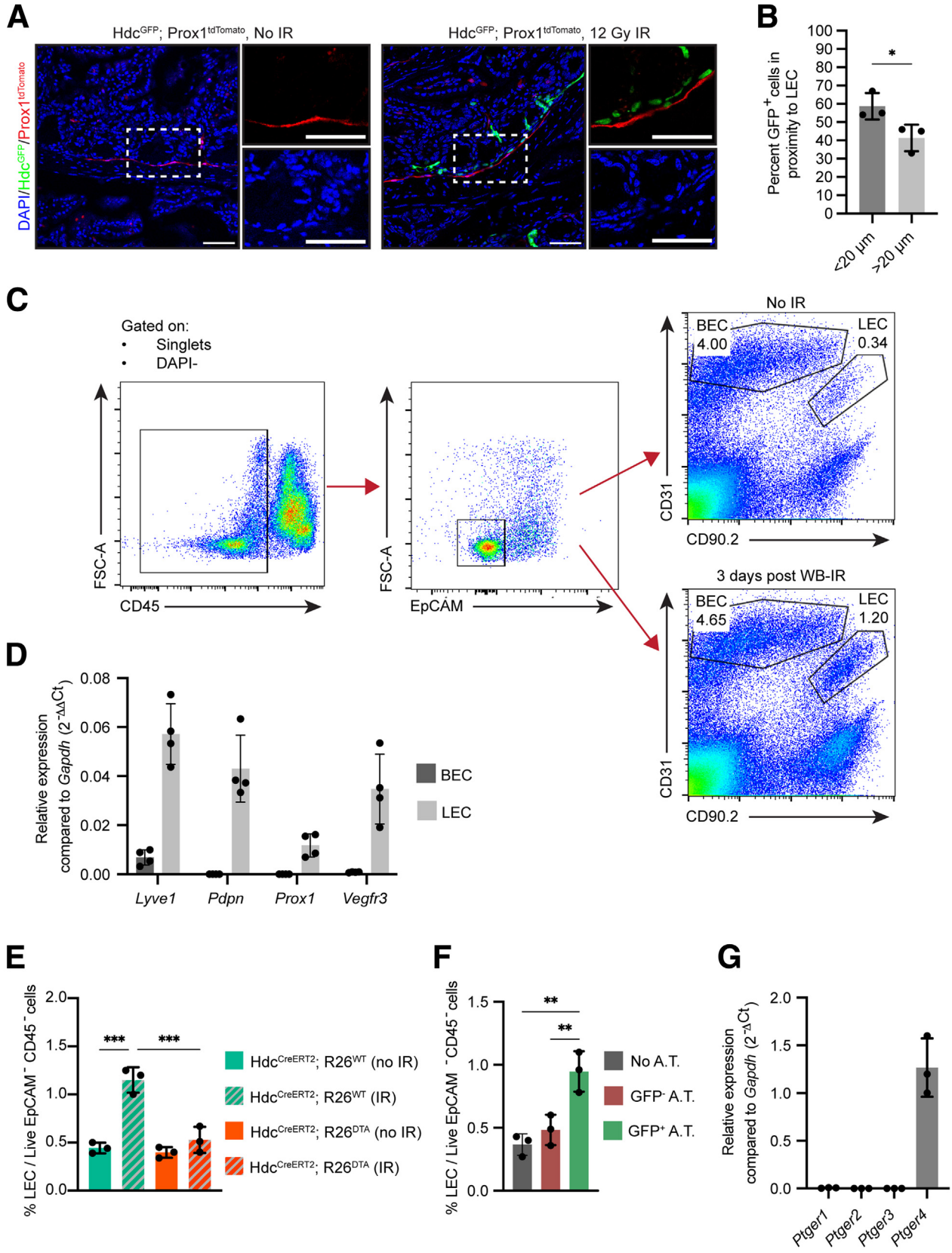
A
HdcGFP; Prox1tdTomato, No IR
HdcGFP; Prox1tdTomato, 12 Gy IR
DAPI/HdcGFP/Prox1tdTomato
B
Percent GFP+ cells in proximity to LEC
<20 µm
>20 µm
C
Gated on:
• Singlets
• DAPI-
FSC-A
CD45
EpCAM
No IR
BEC 4.00
LEC 0.34
CD31
CD90.2
3 days post WB-IR
BEC 4.65
LEC 1.20
D
Relative expression compared to Gapdh (2-ΔΔCt)
BEC
LEC
Lyve1
Pdpn
Prox1
Vegfr3
E
% LEC / Live EpCAM- CD45- cells
HdcCreERT2; R26WT (no IR)
HdcCreERT2; R26WT (IR)
HdcCreERT2; R26DTA (no IR)
HdcCreERT2; R26DTA (IR)
F
% LEC / Live EpCAM- CD45- cells
No A.T.
GFP- A.T.
GFP+ A.T.
G
Relative expression compared to Gapdh (2-ΔCt)
Ptger1
Ptger2
Ptger3
Ptger4

during injury and are a major source of RSPO3.[9,10,13,14] Here, we have shown a crucial role for enteric microbes and immature myeloid cells in regulating intestinal regeneration, in part through modulating LEC activity.

Understanding the mechanism of mucosal repair is crucial for improving therapy for tissue injury. Until now, the involvement of IMCs as a regenerative cell type had been understudied. We report that Hdc^+ IMCs are rapidly recruited to the IR-injured intestine, where they are necessary for proper regeneration. Moreover, we found that the proregenerative effects of Hdc^+ IMCs can be attributed, at least in part, to their secretion of PGE2. In line with previous reports, we found that IMC-derived PGE2 exerts direct mitogenic effects on intestinal epithelial cells.[34,35] Furthermore, we found that PGE2 can act directly on LECs via the EP4 receptor to stimulate lymphangiogenesis and up-regulate the expression of proregenerative genes, such as *Rspo3*, *Ccl21a*, and *Wnt2a*.

Intriguingly, we found that the recruitment of Hdc^+ IMCs to the intestine is initiated by exposure of intestinal lymphatics to invading microbial signals. Specifically, LPS triggers LECs to up-regulate *Cxcl1*, the ligand for CXCR2, which is highly expressed on Hdc^+ IMCs. Treatment of healthy mice with LPS can enforce this recruitment pathway; conversely, clearance of the intestinal microbiome abrogated Hdc^+ IMC recruitment after IR injury, confirming the key role of microbes in triggering IMC migration. These findings suggest that loss of barrier integrity and bacterial infiltration per se are not solely consequences of epithelial damage, but constitute a pathway that initiates intestinal regeneration. Although severe injury and bacterial infiltration may lead to sepsis, moderate levels of microbial exposure appear to promote regenerative signals needed to restore intestinal health and homeostasis. Indeed, the necessity of TLR4 signaling in maintaining intestinal epithelial homeostasis has been described previously, although not in the context of regeneration.[60] Thus, at least in the intestine, microbial signals serve as physiologic signals that can initiate mucosal repair.

Limitations of the Study

In our work, we propose that microbial signals drive a proregenerative axis between intestinal LECs and IMCs after acute whole-body irradiation. It has been reported previously that after exposure to radiation, the bone marrow is suppressed and may fail at higher doses.[61] Given that IMCs originate from the bone marrow and have a crucial role in regulating hematopoiesis,[37] it is possible that some of the effects we observed may be the result of alterations to the bone marrow after IR, especially at the high dose of 12 Gy we used in this study. Thus, the WB-IR model may not fully reflect the circumstances of other types of intestinal injury, and more work should be performed to observe the role of IMCs in other models, such as abdominal irradiation with bone marrow shielding.

In addition, *Hdc* is expressed in other cell types in the body, such as mast cells, enterochromaffin-like cells in the gastric mucosa, and histaminergic neurons in the brain.[43,62,63] Thus, our *Hdc*-driven ablation and conditional knockout models may have produced off-target effects by depleting these cell populations or knocking out their expression of *Ptgs2*. Further studies will need to better parse out the impact on depleting other *Hdc*-expressing cells on intestinal biology.

Another limitation to this study is the use of LPS to simulate the breach of enteric microbes during intestinal barrier disruption. Although this is an established model that has been widely used to study endotoxemia,[58] LPS does not fully recapitulate the diverse signals delivered to the body by invading microbes. It is possible that other bacterial toxins and metabolites are important for signaling the intestinal mesenchyme during barrier disruption, so further studies investigating the crosstalk between microbes and other niche cell populations should be performed to better understand this pathway.

Finally, this study did not investigate the contribution of PGE2 by other cell populations on intestinal lymphatics. Although our data suggest that infiltrating Hdc^+ IMCs are a major source of *Ptgs2* expression and COX-2 signal in the injured intestine, other mesenchymal cell types also express *Ptgs2*, such as tuft cells,[64] pericryptal fibroblasts,[34,35] and macrophages.[29] The contribution of PGE2 from these cells also may signal to lymphatics and promote regeneration, so more experiments investigating the role of PGE2 from each cell population may provide more

Figure 6. (***See previous page***). **Hdc^+ IMCs promote the expansion of LECs after injury.** (*A*) Representative 200× images of Hdc^{GFP} and $Prox1^{tdTomato}$ visualization from the proximal jejunum of Hdc^{GFP}; $Prox1^{tdTomato}$ mice unirradiated (No IR), or after 12-Gy WB-IR. (*B*) Bar plot showing the percentage of Hdc^{GFP} cells in proximity to $Prox1^{tdTomato}$ cells in Hdc^{GFP}; $Prox1^{tdTomato}$ mice 3 days after 12-Gy WB-IR. n = 3. (*C*) Representative FACS plots showing gating strategy for blood endothelial cells (BECs) and LEC isolation from unirradiated mice or mice 3 days after 12-Gy WB-IR. (*D*) Real-time qPCR analysis of sorted BECs and LECs from the jejunum and ileum of unirradiated mice for LEC-related genes. n = 4. (*E*) Quantification of the percentage of CD90.2+ LECs out of all 4′,6-diamidino-2-phenylindole (DAPI)$^-$ $CD45^-$ $EpCAM^-$ cells from the jejunum and ileum of $Hdc^{CreERT2}$; $R26^{DTA}$ or $Hdc^{CreERT2}$; $R26^{WT}$ mice with no irradiation (No IR), and $Hdc^{CreERT2}$; $R26^{WT}$ or $Hdc^{CreERT2}$; $R26^{DTA}$ mice 3 days after 12-Gy WB-IR obtained via FACS. Figure 2*A* shows the experimental scheme. n = 3. (*F*) Bar plot showing quantification of the percentage of LECs from the jejunum and ileum of $Hdc^{CreERT2}$; $R26^{DTA}$ mice after 12-Gy WB-IR that received adoptive transfer of Hdc^{GFP-} bone marrow cells (GFP^- adoptive transfer [A.T.]) or Hdc^{GFP+} bone marrow cells (GFP^+ A.T.) from healthy Hdc^{GFP} mice twice after irradiation, obtained via FACS. Figure 2*K* shows the experimental scheme. n = 3. (*G*) Real-time qPCR analysis of *Ptger* genes of sorted LECs from the jejunum and ileum of unirradiated mice. n = 3. *Scale bars*: 50 μm. $^*P < .05$, $^{**}P < .005$, $^{***}P < .0005$. Bar graph data are means ± SEM. Statistical analysis was performed using a (*B*) 2-sided Student *t* test or an (*E* and *F*) ordinary 1-way analysis of variance with multiple comparisons with each group. FSC-A, forward scatter area. EpCAM, epithelial cellular adhesion molecule.

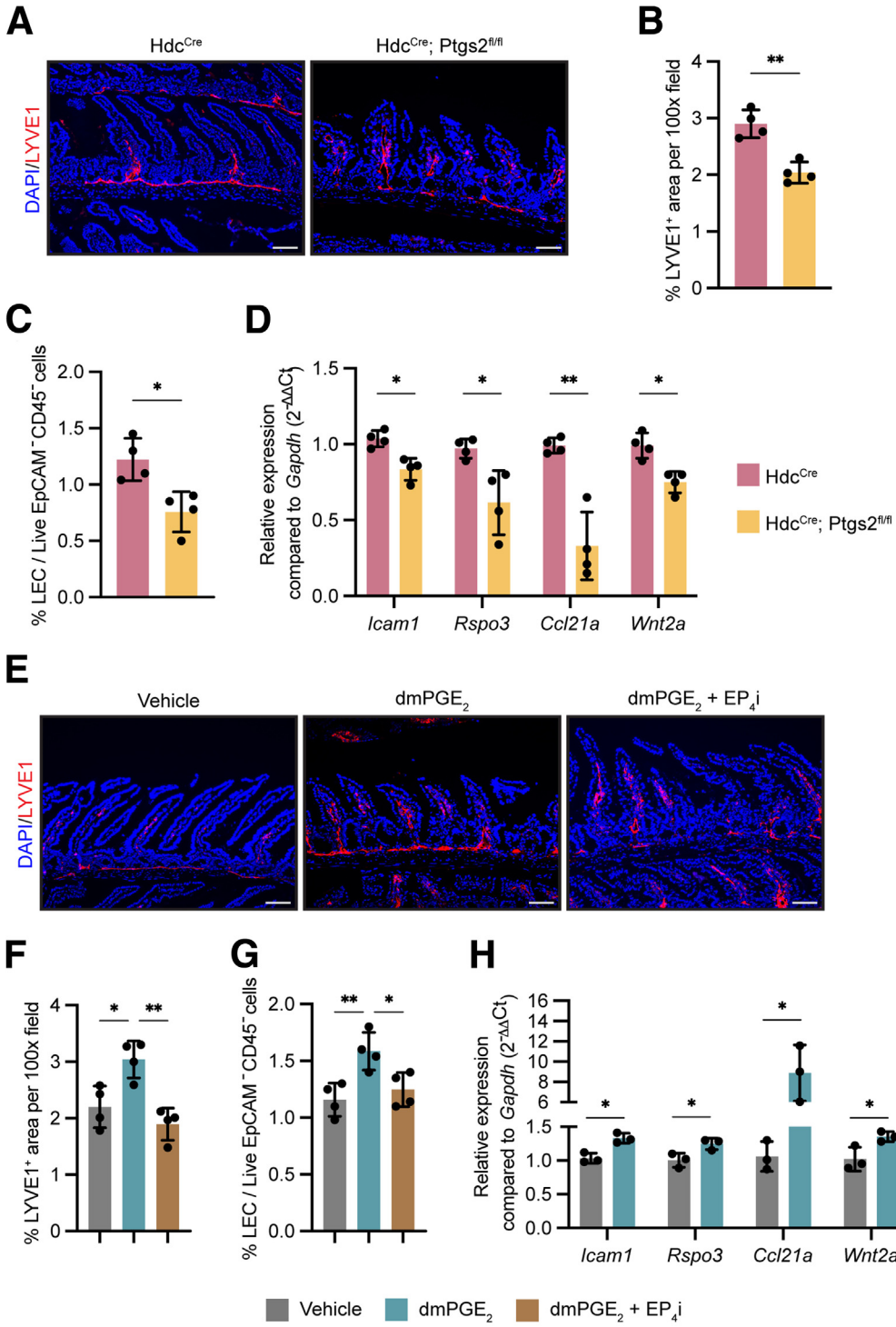

Figure 7. PGE2 from Hdc^{+} IMCs promotes the activation of LECs after injury. (*A*) Representative 100× images of LYVE1 staining from the proximal jejunum of Hdc^{Cre} or Hdc^{Cre}; Ptgs2$^{fl/fl}$ mice after 12-Gy WB-IR. Figure 4*A* shows the experimental scheme. (*B*) Bar plot showing quantification of the average percentage of LYVE1+ area per 100× field of images in panel *A*. n = 4. (*C*) Quantification of the percentage of LECs from the jejunum and ileum of mice after 12-Gy WB-IR. n = 4. (*D*) Real-time qPCR analysis of sorted LECs from the jejunum and ileum of mice after 12-Gy WB-IR. n = 4. (*E*) Representative 100× images of LYVE1 staining from the proximal jejunum of mice after 12-Gy WB-IR. (*F*) Bar plot showing quantification of the average LYVE1+ area per 100× field of images in panel *E*. n = 4. (*G*) Quantification of the percentage of LECs from the jejunum and ileum of mice after 12-Gy WB-IR obtained via FACS. n = 4. (*H*) Real-time qPCR analysis of sorted LECs from the jejunum and ileum of mice after 12-Gy WB-IR. n = 3. *Scale bars*: 50 μm. *$P < .05$, **$P < .005$. Bar graph data are means ± SEM. Statistical analysis was performed using a (*B*, *C*, *D*, and *H*) 2-sided Student *t* test or an (*F* and *G*) ordinary 1-way analysis of variance with multiple comparisons with each group. DAPI, 4′,6-diamidino-2-phenylindole.

insight into how lymphatics are regulated during regeneration.

Materials and Methods

Experimental Model and Subject Details

Mouse crosses and care. All mouse experiments were conducted under the Institutional Animal Care and Use Committee protocols AABE1556 and AABT7651 at the Columbia University Irving Medical Center, and all mouse studies were approved by the Columbia University Institutional Animal Care and Use Committee. For all experiments, male and female mice were used at 8–12 weeks of age at the beginning of each experiment. *Hdc^{GFP}* and *Hdc^{CreERT2}* mice have been described previously.[37,38] *Hdc^{CreERT2}* was mated

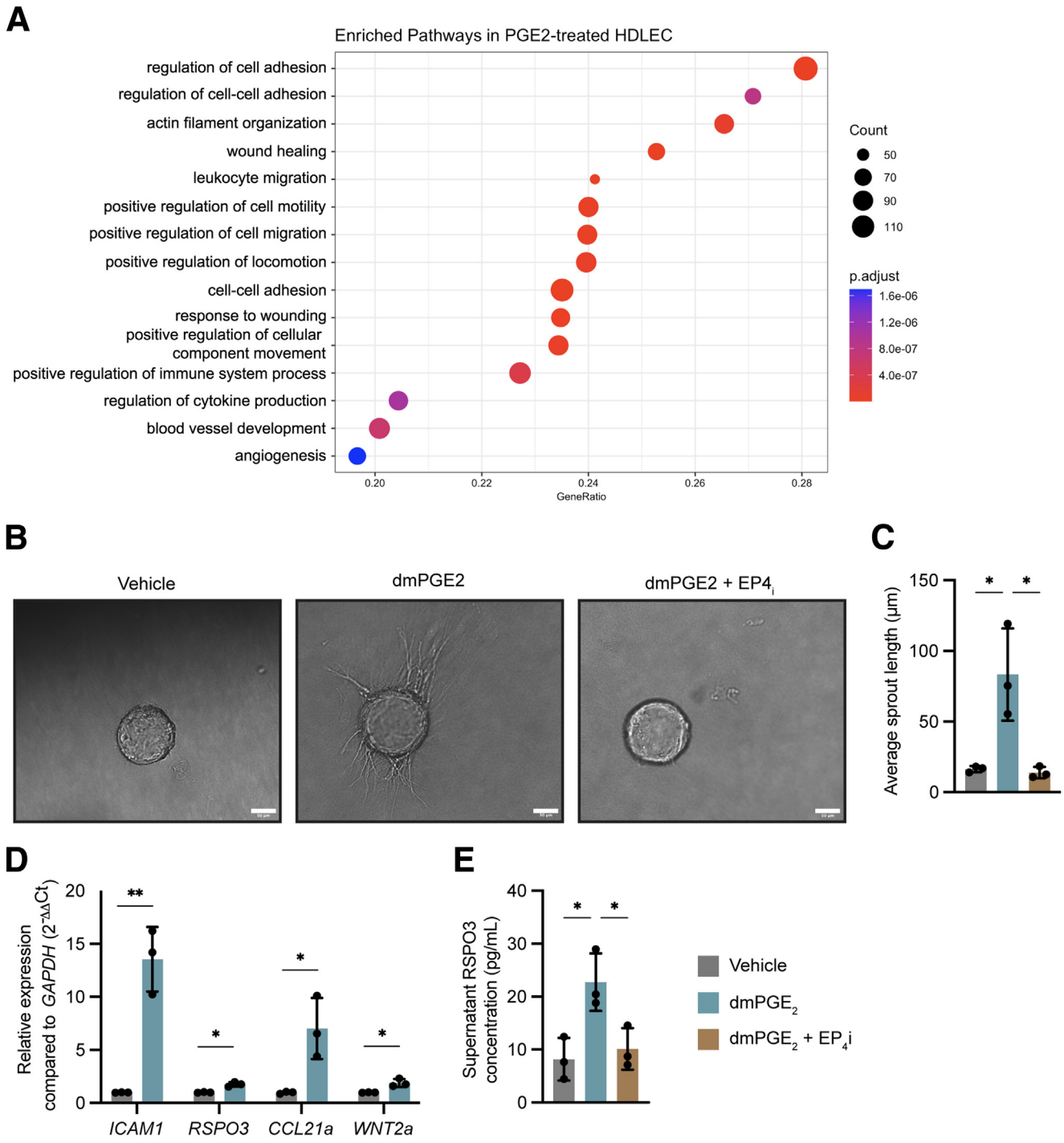

Figure 8. PGE2 promotes lymphangiogenesis of lymphatics. (*A*) Pathway analysis of differentially expressed genes obtained from bulk RNA sequencing of cultured HDLECs treated with PGE2 compared with control. n = 4. (*B*) Representative 200× images of HDLECs on microcarrier beads treated with vehicle, dmPGE2, or dmPGE2 with EP4i. (*C*) Bar plot showing quantification of the average sprout length of panel *B*. n = 3. (*D*) Real-time qPCR analysis of activation and regenerative genes of cultured HDLECs treated with vehicle or dmPGE2 for 6 hours. n = 3. (*E*) Enzyme-linked immunosorbent assay analysis of supernatant RSPO3 isolated from cultured HDLECs treated with vehicle, dmPGE2, or dmPGE2 + EP4i for 16 hours. n = 3. *Scale bar*: 50 μm. Bar graph data are means ± SEM. Statistical analysis was performed using an (*C* and *E*) ordinary 1-way analysis of variance with multiple comparisons with each group or a (*D*) 2-sided Student *t* test. p.adjust, false discovery rate-adjusted p value. **P* < .05, ***P* < .005.

to *Rosa26-DTA* (007909; Jackson Labs) ($R26^{DTA}$) mice for generating $Hdc^{CreERT2}$; $R26^{DTA}$ mice. Hdc^{Cre} mice were purchased from Jackson Labs (021198).[65] $Ptgs2^{fl/fl}$ mice were gifted by Harvey Herschman.[45] Hdc^{Cre} was mated to $Ptgs2^{fl/fl}$ to generate Hdc^{Cre}; $Ptgs2^{fl/fl}$ mice. All mice were maintained in a C57BL/6J background.

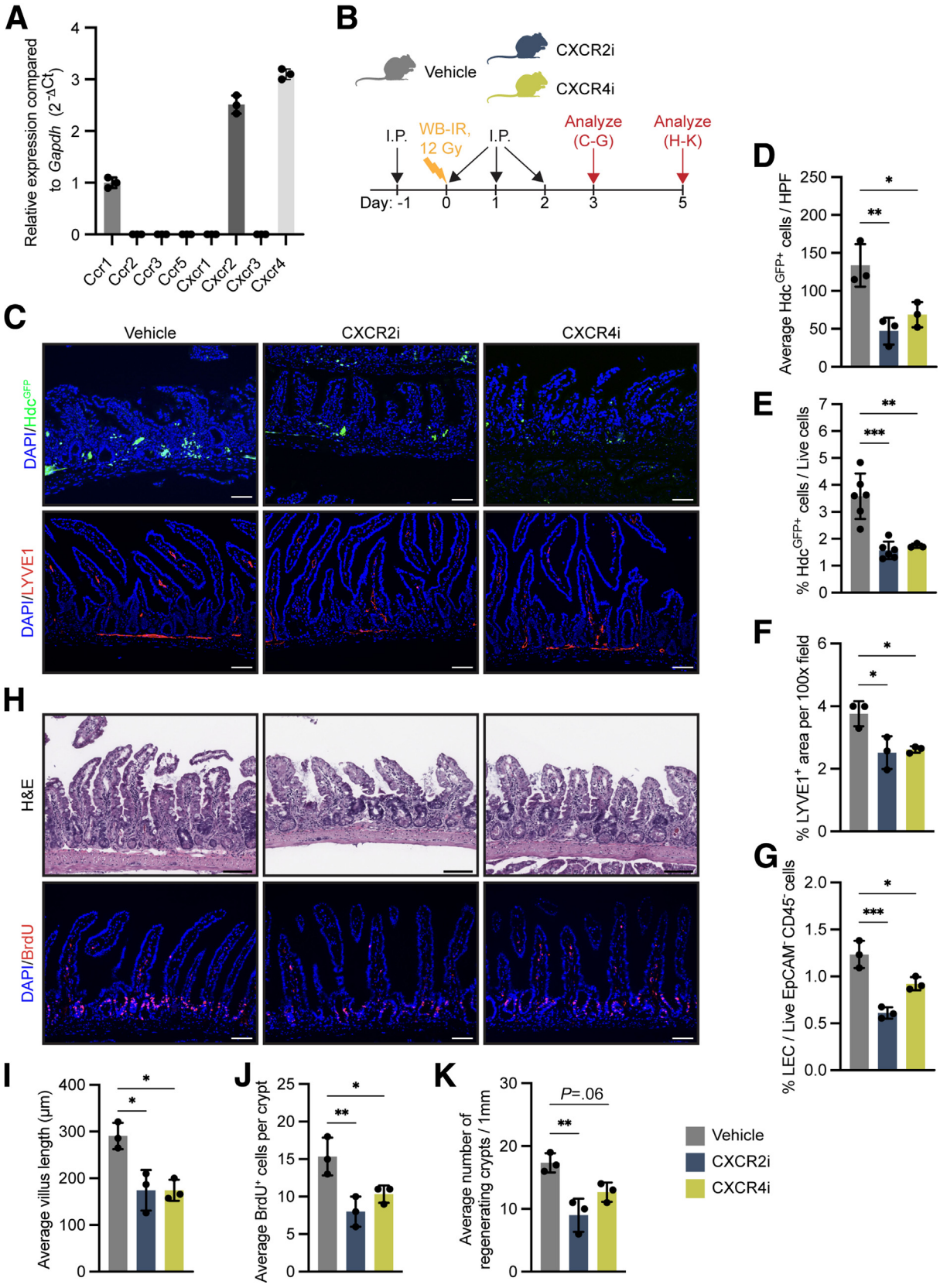
A
Relative expression compared to Gapdh (2^-ΔCt)
Ccr1
Ccr2
Ccr3
Ccr5
Cxcr1
Cxcr2
Cxcr3
Cxcr4
B
Vehicle
CXCR2i
CXCR4i
I.P.
WB-IR, 12 Gy
I.P.
Analyze (C-G)
Analyze (H-K)
Day: -1
0
1
2
3
5
C
Vehicle
CXCR2i
CXCR4i
DAPI/HdcGFP
DAPI/LYVE1
D
Average HdcGFP+ cells / HPF
E
% HdcGFP+ cells / Live cells
F
% LYVE1+ area per 100x field
G
% LEC / Live EpCAM- CD45- cells
H
H&E
DAPI/BrdU
I
Average villus length (μm)
J
Average BrdU+ cells per crypt
K
Average number of regenerating crypts / 1mm
P=.06
Vehicle
CXCR2i
CXCR4i

Mouse drug treatments. Mice were given the CXCR2 inhibitor SB225002 (S7651; Selleck Chemicals) at a dose of 1 mg/kg in phosphate-buffered saline (PBS) + 0.33% Tween 80, or vehicle, intraperitoneally daily for 4 consecutive days. The CXCR4 inhibitor MSX-122 (S6617; Selleck Chemicals) was administered at a dose of 10 mg/kg in PBS + 10% dimethyl sulfoxide + 45% (2-hydroxypropyl)-β-cyclodextrin (332593; Sigma) vehicle, or vehicle, intraperitoneally daily for 4 consecutive days. dmPGE2 (14750; Cayman Chemical Company) was administered intraperitoneally at a dose of 1 mg/kg in PBS + 10% ethanol, or just this vehicle, daily for 3 consecutive days. The EP4-receptor inhibitor L-161,982 (10011565; Cayman Chemical Company) was administered intraperitoneally at a dose of 10 mg/kg in PBS + 10% ethanol 1 hour before dmPGE2 administration. For LPS injections, LPS (tlrl-3pelps; Invivogen) was dissolved in PBS, and this or just PBS was injected intraperitoneally at a dose of 2 mg/kg. For LPS treatment in drinking water, LPS was dissolved in sterile water (10 ug/mL) and given to mice for 7 days. For Hdc^+ cell ablation and Cre activation, mice were fed a tamoxifen diet (delivering 80 mg/kg body weight daily, TD.130858; Envigo) for 2 days before irradiation, and continued the diet until the end of the experiment. The mass of food was monitored daily to ensure that the mice were consuming the proper amount of food to deliver the desired concentration of tamoxifen. For BrdU proliferation experiments, 100 μL BrdU (10 mg/mL, 423401; BioLegend) was injected intraperitoneally into the mice 2 hours before being killed.

Irradiation experiments. Mice were challenged with 12-Gy WB-IR delivered by either a cesium 137 irradiator or a Multirad 350 X-Ray irradiator (Precision X-Ray). Tissue was collected on various days after irradiation.

Antibiotic treatments. Mice were gavaged with an antibiotic cocktail twice a day for 4 days, as published previously.[59] The cocktail consisted of ampicillin (1 g/L, A1593; Sigma), neomycin sulfate (1 g/L, N6386; Sigma), metronidazole (1 g/L, 9002409; Cayman Chemical Company), and vancomycin hydrochloride (0.5 g/L, SBR00001; Sigma). Bacterial depletion was measured using the QIAmp DNA stool mini kit (Qiagen) and following the manufacturer's instructions.

Methods

Tissue collection and preparation for microscopy. For all microscopy experiments, the jejunum was collected, cleaned with PBS, then fixed in 4% paraformaldehyde at 4°C for 24 hours. For sectioning, fixed tissues were embedded in optimal cutting temperature compound (OCT) before being sectioned to a thickness of 4 μm.

Immunohistochemistry, immunofluorescence, and BrdU labeling. For immunofluorescent studies, frozen slides were permeabilized with 1% sodium dodecyl sulfate in PBS at room temperature for 5 minutes, blocked with 10% normal goat serum in 0.1% Tween 20 at room temperature for 1 hour, and stained with primary antibody (rat monoclonal anti-LYVE1, 1:100, 14-0443-82; Thermo Fisher Scientific; rabbit polyclonal anti–COX-2, 1:200, BS-8538R; Bioss Antibodies) at 4°C overnight. Then, sections were incubated with secondary antibodies at room temperature for 2 hours (goat polyclonal anti-rat IgG conjugated to AF 555, 1:400, A-21434; or goat polyclonal anti-rabbit IgG conjugated to AF 555, 1:400, A-21428; Thermo Fisher Scientific). All slides were counterstained and mounted with VECTASHIELD Antiface Mounting Medium with 4′,6-diamidino-2-phenylindole (Vector Laboratories). Fluorescent images were acquired with an X-Cite Series 120 illuminator (Excelitas) on a Nikon Eclipse TE2000-IJ microscope stand (Nikon Instruments). H&E images were acquired with an AT2 microscope slide scanner (Leica), and then processed using QuPath v0.4.[66]

For BrdU fluorescent staining, slides were incubated with 10 mg/mL DNAse I in PBS at 37°C for 20 minutes. Then, BrdU staining was performed as described previously using an anti-BrdU antibody (rat monoclonal anti-BrdU, 1:100, ab6326; Abcam).

Quantification of staining. All image analysis was performed using Fiji software.[67] The average number of Hdc^{GFP+} cells per high-power field was quantified by counting the number of Hdc^{GFP+} cells for 5 randomly selected image fields per mouse, and then averaged. The average number of $BrdU^+$ cells per crypt was quantified by counting the number of $BrdU^+$ cells per crypt for every crypt in 5 separate 100× image fields, and then calculating the mean for each mouse. For the mean villus length, the length of every villus was measured in 5 separate 100× image fields per mouse, and then averaged. The number of regenerating crypts was calculated by counting the number of $BrdU^+$ crypts per 5 different 1 mm continuous stretches per mouse, and then averaged. Lymphatic vessel density was quantified by

Figure 9. (***See previous page***). **Hdc^+ IMCs are recruited to the injured intestine via CXCR2 and CXCR4.** (*A*) RT^2 gene expression analysis for chemokine receptors on isolated Hdc^+ cells from the jejunum and ileum of mice 3 days after 12-Gy WB-IR. n = 3. (*B*) Experimental scheme of CXCR2/CXCR4 inhibition experiment. (*C*) Representative 100× images of GFP visualization (*top*) or LYVE1 staining (*bottom*) from the proximal jejunum of mice from panel *B*. (*D*) Bar plot showing quantification of GFP+ cells of images in panel *C*. n = 3. (*E*) Bar plot showing quantification of FACS analysis of the percentage of Hdc^{GFP+} cells out of live (4′,6-diamidino-2-phenylindole [DAPI]-) cells from the jejunum and ileum of mice from panel *B*. n = 3 or 5. (*F*) Bar plot showing quantification of the average percentage of LYVE1+ area per 100× field of images in panel *C*. n = 3. (*G*) Quantification of the percentage of LECs from the jejunum and ileum of mice from panel *B* obtained via FACS. n = 3. (*H*) Representative 100× images of H&E staining (*top*) and BrdU immunostaining (*bottom*) from the proximal jejunum of mice from panel *B*. (*I*) Bar plot showing quantification of the average villus length from panel *H*. n = 3. (*J*) Bar plot showing quantification of BrdU staining from panel *H*. n = 3. (*K*) Bar plot showing quantification of the average number of regenerating crypts per 1 mm from panel *H*. n = 3. Mice were analyzed (*C–G*) 3 days after WB-IR or (*H–K*) on day 5. Bar graph data are means ± SEM. (*D–G* and *I–K*) Statistical analysis was performed using an ordinary 1-way analysis of variance with multiple comparisons with each group. *Scale bars*: 50 μm. *$P < .05$, **$P < .005$, and ***$P < .0005$. HPF, high-power field; IP, intraperitoneal injection of vehicle, SB225002 (CXCR2i), or MSX-122 (CXCR4i).

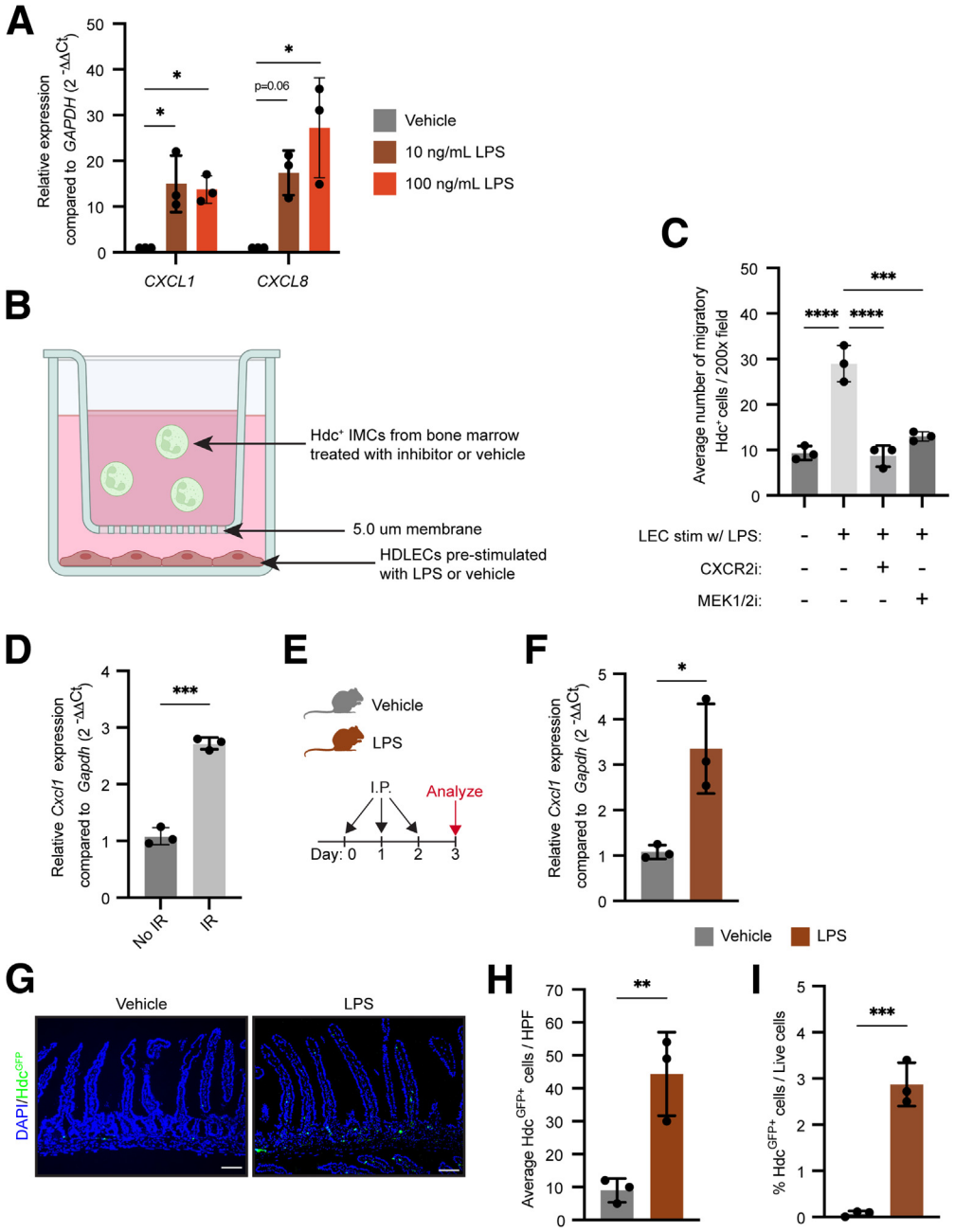

Figure 10. Microbial signals promote LEC recruitment of Hdc^{+} IMCs. (*A*) Real-time qPCR for *CXCL1* and *CXCL8* in cultured HDLECs treated with various LPS concentrations for 6 hours. n = 3. (*B*) Scheme of Transwell migration assay. (*C*) Quantification of results of Transwell migration assay. n = 3. CXCR2i, SB225002; MEK1/2i, U0126. (*D*) Real-time qPCR analysis of sorted LECs from the jejunum and ileum of unirradiated mice or mice 3 days after 12-Gy WB-IR. n = 3. (*E*) Experimental scheme of LPS injection experiment. (*F*) Real-time qPCR analysis of sorted LECs from the jejunum and ileum of mice from panel *E*. n = 3. (*G*) Representative 100× images of GFP visualization from the proximal jejunum of mice from panel *E*. (*H*) Bar plot showing quantification of Hdc^{GFP+} cells of images in panel *G*. n = 3. (*I*) Bar plot showing quantification of FACS analysis of the percentage of Hdc^{GFP+} cells of mice from panel *E*. n = 3. *Scale bars*: 50 μm. Bar graph data are means ± SEM. Statistical analysis was performed using an (*A* and *C*) ordinary 1-way analysis of variance with multiple comparisons with each group or a (*D*, *F*, *H*, and *I*) 2-sided Student *t* test. *$P < .05$, **$P < .005$, ***$P < .0005$, ****$P < .00005$. DAPI, 4′,6-diamidino-2-phenylindole; HPF, high-power field; IP, intraperitoneal injection of vehicle or LPS. MEK1/2, mitogen-activated kinase kinase 1/2.

measuring the average LYVE-1–positive area out of the total area for 5 separate 100× image fields per mouse. Images seen in figures are all composites of different channels unless otherwise stated.

Small intestine tissue digestion and flow cytometry analysis. Lymphatic cells were isolated from the small intestine as previously described.[14,68] Briefly, the entire small intestine from adult male and female mice was

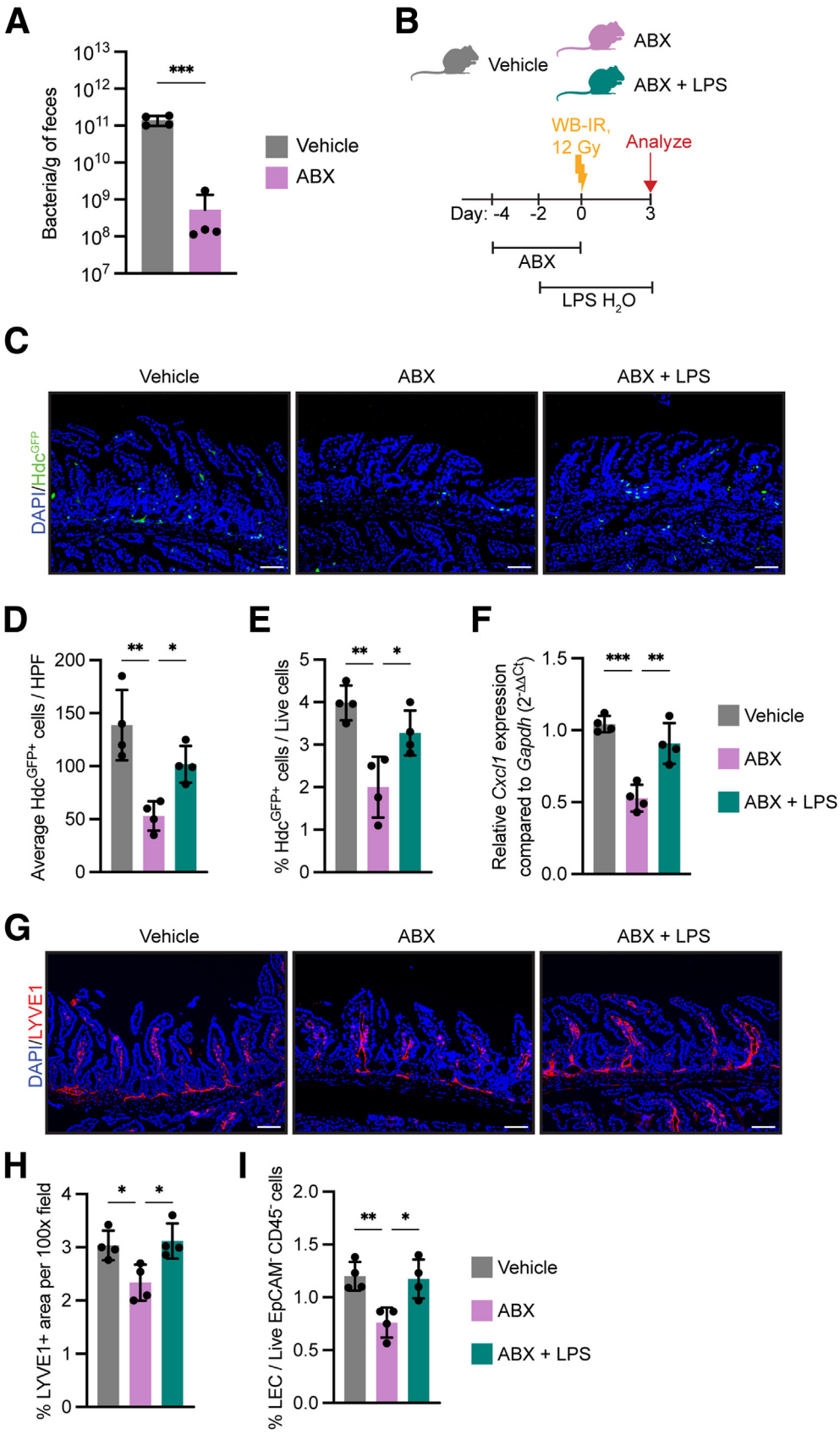

Figure 11. Microbial signals modulate the cross-talk between Hdc^{+} IMCs and LECs. (*A*) Bar plot showing quantification of fecal bacterial load from mice gavaged with vehicle or an antibiotic cocktail (ABX). (*B*) Experimental scheme of antibiotic and LPS experiment. ABX indicates an antibiotic gavage was administered twice daily. LPS H_2O indicates that LPS was added to the drinking water. n = 4. (*C*) Representative 100× images of GFP visualization from the proximal jejunum of mice from panel *B*. (*D*) Bar plot showing quantification of GFP+ cells of images in panel *C*. n = 4. (*E*) Bar plot showing quantification of FACS analysis of the percentage of Hdc^{GFP+} cells out of live (4′,6-diamidino-2-phenylindole [DAPI]-) cells from the jejunum and ileum of mice from panel *B*. n = 4. (*F*) Real-time qPCR analysis of *Cxcl1* in sorted LECs from the jejunum and ileum of mice from panel *B*. n = 4. (*G*) Representative 100× images of LYVE1 staining from the proximal jejunum of mice from panel *B*. (*H*) Bar plot showing quantification of the average LYVE1+ area per 100× field of images in panel *G*. n = 4. (*I*) Quantification of FACS analysis of the percentage of LECs from the jejunum and ileum of mice from panel *B*. n = 4. *Scale bars*: 50 μm. Bar graph data are means ± SEM. Statistical analysis was performed using a (*A*) 2-sided Student *t* test or an (*D–F*, *H*, and *I*) ordinary 1-way analysis of variance with multiple comparisons with each group. **P* < .05, ***P* < .005, and ****P* < .0005. EpCAM, epithelial cellular adhesion molecule; HPF, high-power field.

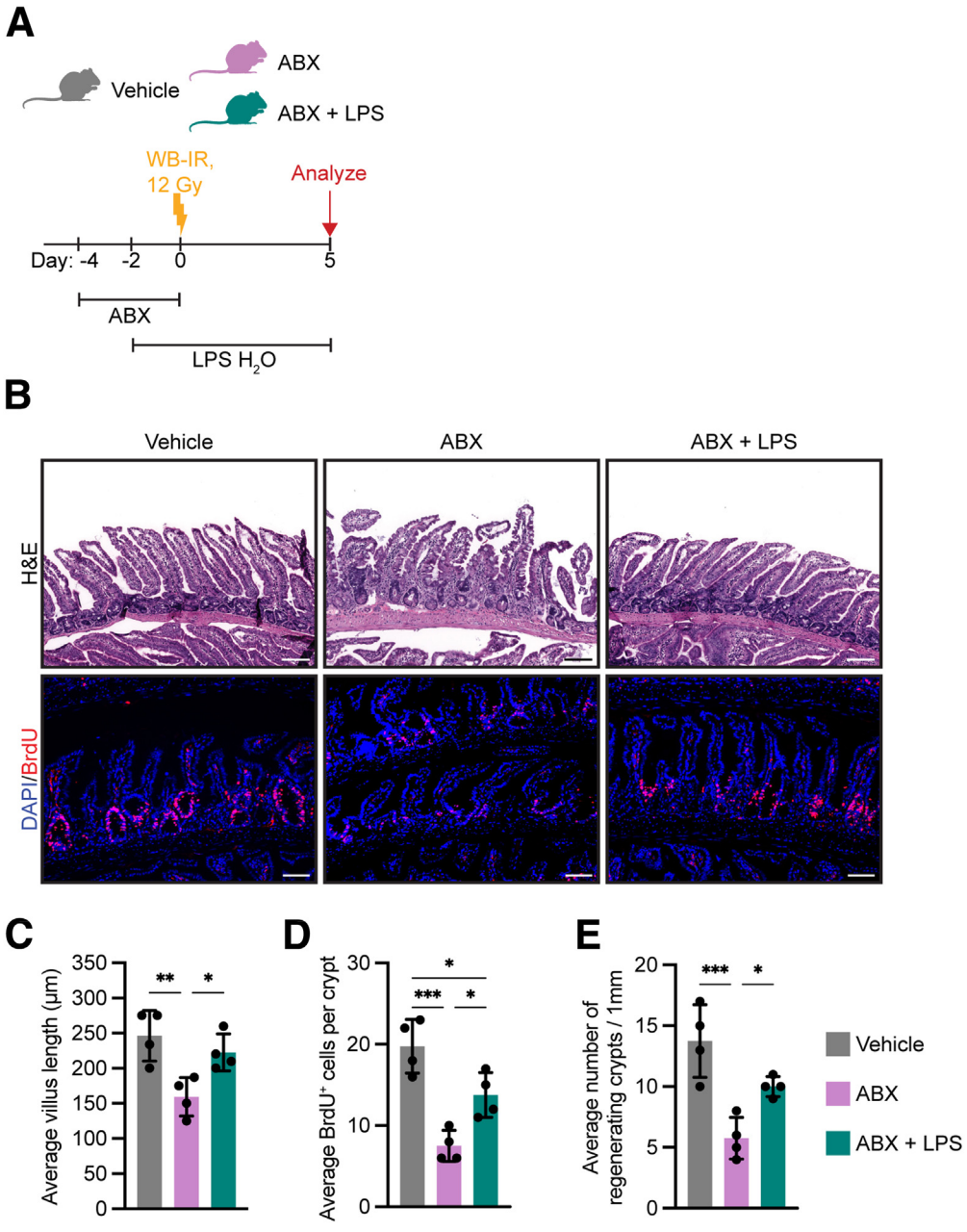

Figure 12. Microbial signals promote intestinal regeneration after injury. (*A*) Experimental scheme of antibiotic and LPS experiment. Antibiotic gavage was administered twice daily. LPS was added to the drinking water (LPS H_2O). (*B*) Representative 100× images of H&E (*top*) and BrdU (*bottom*) staining from the proximal jejunum of mice from panel *A*. (*C*) Bar plot showing quantification of the average villus length from images in panel *B*. n = 4. (*D*) Bar plot showing quantification of BrdU staining from images in panel *B*. n = 4. (*E*) Bar plot showing quantification of the average number of regenerating crypts per 1 mm from images in panel *B*. n = 4. *Scale bars*: 50 μm. Bar graph data are means ± SEM. (*C–E*) Statistical analysis was performed using an ordinary 1-way analysis of variance with multiple comparisons with each group. **P* < .05, ***P* < .005, and ****P* < .0005. ABX, antibiotic cocktail.

collected, the duodenum was removed, and then the tissue was flushed with cold PBS and dissected to remove mesentery and fat tissue. Then, the tissue was turned inside out, the mucus was removed with a paper towel, and the tissue was cut into approximately 1-mm pieces. The pieces were put into 30 mL dissociation solution (RPMI 1640 with L-glutamine, 11875-119; Thermo Fisher) + 1% nonessential amino acids (11140050; Thermo Fisher), 2.5% HEPES (H3662; Sigma), 1% antibiotic–antimycotic (15240062; Thermo Fisher), 5 mmol/L EDTA (11575-038; Thermo Fisher), 3% fetal bovine serum (900-108; Gemini Bio-Products) and 1 μmol/L dithiothreitol (43816; Sigma), and incubated on a rotator at 37°C for 30 minutes. Then, the tissues were strained through a 100-μm cell strainer, washed twice with Hank's balanced salt solution (HBSS), and minced finely using scissors. The minced tissue then was placed in 25 mL digestion media (HBSS + 1% GlutaMAX, 1% nonessential amino acids, and 2.5% HEPES with 2.5 mg/mL Collagenase II, LS004176; Worthington), 1 U/mL Dispase II (D4693; Sigma), and 30 μg/mL DNAse I (10104159001; Sigma), and incubated at 37°C for 15 minutes on a rotator. The solution was passed through a 14-gauge needle 5 times using a syringe, then placed back on the rotator to digest for 15 more minutes at 37°C. The digested cells were strained through a 100-μm strainer, and any remaining tissue was digested again for 30 more

minutes. The cell suspensions were mixed, pelleted, then placed in 5 mL 1× RBC lysis buffer (420301; BioLegend) for 5 minutes on ice. The reaction was quenched with PBS, then spun down, and the remaining single-cell suspension was incubated with TruStain FcX (101319; BioLegend) for 5 minutes on ice. Finally, the suspension was stained with the following antibody cocktail: CD45-Pacific Blue (1:200, 103125; BioLegend), TER119-Pacific Blue (1:200, 116231; BioLegend), Ep-CAM-APC-Cy7 (1:200, 118217; BioLegend), CD31-PE (1:500, 160203; BioLegend), Lyve1-PE-CY7 (1:300, 25-0443-82; eBioscience), and CD90.2-BV605 (1:300, 105343; BioLegend). Propidium iodide (421301; BioLegend) or 4′,6-diamidino-2-phenylindole (422801; BioLegend) was used as a viability dye to exclude dead cells from the analysis. Cells were analyzed on a NovoCyte Quanteon or sorted using a Sony MA900 with a 100-micron nozzle. GFP^+ cells were defined as prodidium iodide $(PI)^-$, GFP^+. Lymphatic endothelial cells were defined as PI^-, $Ep\text{-}CAM^-$, $CD45^-$, $CD31^+$, $CD90.2^+$, $LYVE1^+$. For RNA isolation, cells were sorted directly into TRIzol LS (10296028; Thermo Fisher). The data were analyzed using FlowJo software (version 10; TreeStar).

Bone marrow cell isolation. HDC^+ bone marrow cells were obtained from Hdc^{GFP} mice by crushing leg, arm, and pelvic bones in HBSS containing 2% heat-inactivated fetal bovine serum (900-108; Gemini). Single-cell suspensions were purified on a Ficoll gradient (17544202; Cytiva), and then red blood cells were lysed using 1× RBC lysis buffer (420301; BioLegend). The cells were stained with the following antibody cocktail: CD45-AF 700 (1:800, 103127; BioLegend), CD11b-PE-Cy7 (1:800, 101215; BioLegend), and Gr-1–APC (1:400, 108411; BioLegend). Propidium iodide was used as a viability dye to exclude dead cells. Cells were sorted using a Sony MA900 with a 100-micron nozzle. $CD45^+$, $CD11b^+$, $Gr\text{-}1^+$, and GFP^+ cells were sorted directly into X-VIVO 15 media (04-418Q; Lonza) for further culture experiments, or directly into TRIzol LS for RNA isolation.

Adoptive transfer. $HdcCre^{ERT2}$; $R26^{DTA}$ mice were placed on a tamoxifen diet for 2 days, then were challenged with 12-Gy WB-IR. $CD11b^+$ Hdc^{GFP+} or $CD11b^+$ Hdc^{GFP-} myeloid cells were isolated from the bone marrow of 3 healthy Hdc^{GFP} gender-matched, littermate donor mice and pooled. Six hours after WB-IR, $HdcCre^{ERT2}$; $R26^{DTA}$ recipient mice were injected with 3 million $CD11b^+$ Hdc^{GFP+} or $CD11b^+$ Hdc^{GFP-} cells via the tail vein, and this was repeated 72 hours later. Samples were collected 6 days after WB-IR.

In vitro organoids. The entire small intestine from 8- to 12-week-old male and female mice was collected, and then the duodenum was removed. The remaining tissue was flushed with cold PBS, cleaned of the mesentery, and opened lengthwise. EDTA-based (15575020; Invitrogen) dissociation was performed as previously described.[69] After EDTA dissociation, crypts were resuspended in Advanced Dulbecco's modified Eagle medium/F12 (12634-010; Gibco) supplemented with GlutaMAX (35050061; Thermo Fisher Scientific), HEPES (15-630-080; Thermo Fisher Scientific), antibiotic–antimycotic (15240062; Fisher Scientific), 10% fetal bovine serum (900-108; Gemini Bio-Products), B27 (17504044; Thermo Fisher Scientific), N-2 supplement (17502048; Fisher Scientific), N-acetyl-L-cysteine (A9165; Sigma-Aldrich), EGF (PMG8043; Thermo Fisher Scientific), Noggin (250-38; PeproTech), Rspo1 (3474-RS-050; R&D Systems), and CHIR (SML1046; Sigma-Aldrich). Crypts were counted under a microscope, and then 200 crypts were seeded into 20 uL GFR Matrigel (356231; Corning) and plated in a prewarmed 24-well plate as domes. dmPGE2 and/or EP4i treatment began 24 hours after plating, and media was replaced every 2 days. Organoid size and number data were collected on day 6 after plating.

HDLEC cell culture. HDLECs from juvenile foreskin were purchased from Promocell (C-12216) and cultured in Endothelial Cell Growth Media MV2 (C22121; Promocell). Cells were maintained in a humidified incubator set to 37°C and 5% CO_2. For PGE2 stimulation experiments, 3×10^5 cells per well were plated in a 12-well plate and allowed to seed overnight. dmPGE2 was added to a concentration of 500 nmol/L or 1 μmol/L, and L-161,982 was added to a concentration of 2 μmol/L. For gene expression analysis, the cells were treated for 6 hours, lysed with Buffer RLT Plus (Qiagen), and then RNA was collected using the RNEasy Plus Mini Kit (74134; Qiagen). For quantification of supernatant RSPO3, the cells were treated for 18 hours and then the supernatant was harvested for enzyme-linked immunosorbent assay analysis. For LPS stimulation, 3×10^5 cells per well were plated in a 12-well plate and allowed to seed overnight. Ultrapure LPS (tlrl-3pelps; Invivogen) was added at a concentration of 1, 10, or 100 ng/mL and the cells were incubated for 6 hours before being harvested for RNA isolation or migration analysis.

HDLEC sprouting assay. An endothelial cell assay was performed as described previously.[50] Briefly, Cytodex 3 microcarrier beads (17048502; Cytiva) were coated by adding 10^6 detached HDLECs to 1200 beads suspended in PBS. The bead–cell suspension was incubated at 37°C for 4 hours, agitating every 20 minutes. Then, the coated beads were plated on a 6-cm plate in Endothelial Cell Growth Media MV2 overnight. The next morning, the beads were inspected under a microscope to ensure consistent coating of the beads. The beads were washed, resuspended in a fibrinogen solution (F8630; Sigma), and then plated into thrombin (T4648; Sigma) to form a fibrin gel in a 24-well glass-bottomed plate. Once the gel was fully solidified, the cells were treated with control media or media containing dmPGE2 at a concentration of 1 μmol/L with or without L-161,982, at a concentration of 2 μmol/L. The media was changed after 24 hours, and then the cells were inspected for sprouting under a microscope 48 hours after implantation into the gel. The average sprout length per group was calculated by measuring the length of every sprout coming off 5 different beads per well, and then calculating the mean.

HDC^+ cell and HDLEC co-culture and migration assays. For migration analyses, HDLECs that had been stimulated with 0, 1, 10, or 100 ng/mL LPS were detached using a DetachKit (C-41200; PromoCell), pelleted, then washed twice with PBS. Cells (5×10^4) were plated in the bottom well of a 96-well Transwell plate with 5.0-μm pores (3387; Corning), and allowed to seed overnight. The CXCR2 inhibitor SB225002 was added to some of the HDLEC-

Table 1. qPCR Primer Sequences for Mouse Genes

Gene	Forward sequence, 3'–5'	Reverse sequence, 3'–5'
Gapdh	AGGTCGGTGTGAACGGATTTG	TGTAGACCATGTAGTTGAGGTC
Ptgs2	TTCAACACACTCTATCACTGGC	AGAAGCGTTTGCGGTACTCAT
Rspo3	ATGCACTTGCGACTGATTTCT	GCAGCCTTGACTGACATTAGGAT
Icam1	GTGATGCTCAGGTATCCATCCA	CACAGTTCTCAAAGCACAGCG
Ccl21a	AAGGCAGTGATGGAGGGGGT	CTTAGAGTGCTTCCGGGGTG
Wnt2a	CTCGGTGGAATCTGGCTCTG	CACATTGTCACACATCACCCT
Reln	GGACTAAGAATGCTTATTTCC	GGAAGTAGAATTCATCCATCAG
Lyve1	TAGCTTTGAAACTTGCAGCTATG	TCAACAAATGGTTCAGTTTCTGTAG
Prox1	ACGTAAAGTTCAACAGATGCATTAC	CCAGCTTGCAGATGACCTTG
Vegfr3	GAGACCTGGCTGCTCGGAAC	TCAGCATGATGCGGCGTATG
Pdpn	CCCAGGAGAGCAACAACTCAAC	CTCGATGCGAATGCCTGTTAC

containing wells at a concentration of 200 nmol/L, or the mitogen-activated protein kinase kinase 1/2 (MEK1/2) inhibitor U0126 (S1102; Selleck Chemicals) was added to some wells at a concentration of 5 μmol/L. Sorted HDC^{+} immature myeloid bone marrow cells (10^4) from Hdc^{GFP} mice were placed in the upper insert of the Transwell, and the plate was incubated for 12 hours. The top insert was discarded, and the average number of migratory cells per 200× field was calculated by counting the number of GFP^{+} cells for 5 independent 200× fields per bottom well and then calculating the average.

Enzyme-linked immunosorbent assay. The concentration of RSPO3 was measured using the human R-Spondin-3 Picokine enzyme-linked immunosorbent assay Kit (EK1512; Boster Bio) according to the manufacturer's instructions. HDLEC-conditioned media (18 hours after treatment with vehicle or dmPGE2 with or without L-161,982) was used at 1, 1:2, and 1:4 serial dilutions. The protein concentration was measured at 450 nm on a SpectraMax iD3 Microplate Reader (Molecular Devices).

RNA isolation and complementary DNA synthesis. RNA was isolated from fresh whole tissue, tissue that had been preserved in RNAlater (AM7020; Invitrogen), or cell pellets. A total of 5–10 mg distal jejunum tissue from control or irradiated Hdc^{GFP} mice treated with dmPGE2 with or without L-161,982 was homogenized using metal beads in a Bullet Blender Tissue Homogenizer (Next Advance). The resulting homogenate was dissolved in Buffer RLT Plus (Qiagen) and RNA was isolated using the RNEasy Plus Micro kit (74030; Qiagen) according to the manufacturer's instructions, including genomic DNA elimination. The final elution volume was 14 or 30 μL, and RNA quantity and quality were measured on a NanoDrop 8000 spectrophotometer (Thermo Fisher). For RNA isolation from sorted bone marrow or small intestinal lymphatic endothelial cells, 1–5 × 10^5 cells were sorted directly into TRIzol LS. RNA then was isolated via chloroform phase separation and isopropanol precipitation. RNA from cultured HDLECs was collected by lysing 80%–90% confluent cells seeded on a 12-well plate in 500 mL Buffer RLT Plus, and then homogenized using a QIAshredder column. The same amount of RNA (up to 1 ug) was loaded per sample for subsequent complementary DNA (cDNA) synthesis. cDNA was synthesized by loading at least 100 ng RNA per sample and using the qScript cDNA Supermix (Quantabio). Briefly, in a final volume of 20 μL, the qScript Supermix (5×) was mixed with

Table 2. qPCR Primer Sequences for Human Genes

Gene	Forward sequence, 3'–5'	Reverse sequence, 3'–5'
GAPDH	CAAGAGCACAAGAGGAAGAGAG	CTACATGGCAACTGTGAGGAG
PTGER1	GGGCTTAACCTGAGCCTAGC	GTGATGTGCCATTATCGCCTG
PTGER2	CGATGCTCATGCTCTTCGC	GGGAGACTGCATAGATGACAGG
PTGER3	CGCCTCAACCACTCCTACAC	GACACCGATCCGCAATCCTC
PTGER4	CCGGCGGTGATGTTCATCTT	CCCACATACCAGCGTGTAGAA
ICAM1	TCAGCCTGAGCTACAGATGC	CTTTAGCTTCGGGTCAATGC
RSPO3	GGAGTGTGTCAGTATTGTGCACTG	GCTTCTTCTGCTGCTGTTTGTT
CCL21a	GTTGCCTCAAGTACAGCCAAA	AGAACAGGATAGCTGGGATGG
WNT2a	GCTGGAATTGCAACACCCTG	ACCGCTTTACAGCCTTCCTG
CXCL1	GCGCCCAAACCGAAGTCATA	ATGGGGGATGCAGGATTGAG
CXCL8	AAGAGAGCTCTGTCTGGACC	GATATTCTCTTGGCCCTTGG

Table 3. Materials Table

Reagent or resource	Source	Identifier
Antibodies		
Alexa Fluor 700 anti-mouse CD45	BioLegend	Cat# 157210; RRID: AB_2860730
Alexa Fluor 700 anti-mouse Ly6G	BioLegend	Cat# 127621; RRID: AB_10640452
APC anti-mouse Ly-6C	BioLegend	Cat# 128015; RRID: AB_1732087
APC anti-mouse Ly-6G/Ly-6C (Gr-1)	BioLegend	Cat# 108411; RRID: AB_313376
APC/Cyanine 7 anti-mouse CD326 (Ep-CAM) antibody	BioLegend	Cat# 118217; RRID: AB_1501158
APC/Cyanine7 anti-mouse FcepsilonR1alpha antibody	BioLegend	Cat# 134325; RRID: AB_2572063
Brilliant Violet 605 anti-mouse CD90.2 (Thy1.2) antibody	BioLegend	Cat# 140318; RRID: AB_2650924
Brilliant Violet 785 anti-mouse CD117 (c-kit)	BioLegend	Cat# 105841; RRID: AB_2629799
Goat polyclonal anti-rabbit horseradish peroxidase	Thermo Fisher	Cat# 32260; RRID: AB_1965959
Goat polyclonal anti-rat AF 555	Thermo Fisher	Cat# A-21434; RRID: AB_2535855
Goat polyclonal anti-rabbit AF 555	Thermo Fisher	Cat# A-21428; RRID: AB_2535849
Pacific Blue anti-mouse CD45 antibody	BioLegend	Cat# 103126; RRID: AB_493535
PE anti-mouse CD123 antibody	BioLegend	Cat# 106005; RRID: AB_2124403
PE anti-mouse CD31 antibody	BioLegend	Cat# 102508; RRID: AB_312915
PE-Cyanine 7 anti-mouse LYVE1	Thermo Fisher	Cat# 25-0443-82; RRID: AB_2802237
PE/Cyanine 7 anti-mouse/human CD11b	BioLegend	Cat# 101215; RRID: AB_312798
PerCP/Cyanine 5.5 anti-mouse CD193 (CCR3) antibody	BioLegend	Cat# 144515; RRID: AB_2565741
Rabbit monoclonal anti-Ki67	Abcam	Cat# ab16667; RRID: AB_302459
Rat monoclonal anti-BrdU	Abcam	Cat# ab6326; RRID: AB_305426
Rat monoclonal anti-LYVE1	Thermo Fisher	Cat# 14-0443-82; RRID: AB_1633414
Rabbit polyclonal anti–COX-2	Bioss	Cat# bs-0732R; RRID: AB_10859004
Chemicals, peptides, and recombinant proteins		
(2-Hydroxypropyl)-β-cyclodextrin	Sigma	Cat# 332593
10% neutral buffered formalin	VWR	Cat# 16004
16, 16-dimethyl prostaglandin E_2 (dmPGE2)	Cayman Chemical Company	Cat# 14750
32% paraformaldehyde	Electron Microscopy Services	Cat# 15714
5-Bromo-2'-deoxyuridine (BrdU)	BioLegend	Cat# 423401
Advanced Dulbecc''s modified Eagle medium/F12	Gibco	Cat# 12634-010
Ampicillin	Sigma	Cat# A1593
Antibiotic–antimycotic (anti-anti)	Thermo Fisher	Cat# 15240062
B27	Thermo Fisher	Cat# 17504044
Bovine serum albumin	Sigma	Cat# A9418
Cell staining buffer	BioLegend	Cat# 420201
CHIR	Sigma	Cat# SML1046
Collagenase II	Worthington	Cat# LS004176
Cytodex 3 Microcarrier Beads	Cytiva	Cat# 17048502
Dako Liquid DAB+ Substrate Chromogen System	Agilent Technologies	Cat# K3468
DAPI	BioLegend	Cat# 422801
DetachKit	Promocell	Cat# C-41200
Dispase II	Sigma	Cat# D4693
DNAse I	Sigma	Cat# 10104159001
DPBS, no calcium, no magnesium	Gibco	Cat# 141190250
DTT	Sigma	Cat# 43816
EDTA	Thermo Fisher	Cat# 11575-038
EGF	Thermo Fisher	Cat# PMG8043
Endothelial Cell Growth Media MV2	Promocell	Cat# C22121
Fetal bovine serum	Gemini Bio-Products	Cat# 900-108
Fibrinogen from bovine plasma, type I-S	Sigma	Cat# F8630
Ficoll-Paque Premium	Cytiva	Cat# 17544202
GFR Matrigel	Corning	Cat# 356231
GlutaMAX	Gibco	Cat# 35050-061
HBSS	Gibco	Cat# 14175-095
HEPES	Sigma	Cat# H3662
ImmPACT DAB Substrate Kit	Vector Laboratories	Cat# SK-4105
L-161,982 (EP4i)	Cayman Chemical Company	Cat# 10011565
LPS ultrapure	Invivogen	Cat# tlrl-3pelps
Metronidazole	Cayman Chemical Company	Cat# 9002409
Molecular biology grade water	Corning	Cat# 46-000-CV
MSX-122 (CXCR4i)	Selleck Chemicals	Cat# S6617
N-2 supplement	Thermo Fisher	Cat# 17502048
N-acetyl-L-cysteine	Sigma	Cat# A9165
Neomycin sulfate	Sigma	Cat# N6386
Noggin	PeproTech	Cat# 250-38
Nonessential amino acids	Thermo Fisher	Cat# 11140050
Normal goat serum	Vector Laboratories	Cat# S-1000
PerfeCTa SYBR Green FastMix, Low ROX	VWR	Cat# 101414-286
Propidium iodide	BioLegend	Cat# 421301
Qscript cDNA Supermix	VWR	Cat# 101414-108

Table 3. Continued

Reagent or resource	Source	Identifier
RBC lysis buffer (10X)	BioLegend	Cat# 420301
RNA*later*	Thermo Fisher	Cat# AM7020
RPMI 1640 with L-glutamine	Thermo Fisher	Cat# 11875-119
Rspo1	R&D Systems	Cat# 3474-RS-050
SB225002 (CXCR2i)	Selleck Chemicals	Cat# S7651
SDS	Thermo Fisher	Cat# BP166-500
Thrombin from bovine plasma	Sigma	Cat# T4648
Triton X-100	Thermo Fisher	Cat# BP151-500
TRIzol LS	Thermo Fisher	Cat# 10296028
TruStain FcX	BioLegend	Cat# 101319
TWEEN 20	Sigma	Cat# D8418
TWEEN 80	Sigma	Cat# P1754
U0126 (MEK1/2i)	Selleck Chemicals	Cat# S1102
Vancomycin	Sigma	Cat# SBR00001
VECTASHIELD Antifade Mounting Medium with DAPI	Vector Laboratories	Cat# H-1200
X-VIVO 15 media	Lonza	Cat# 04-418Q
Critical commercial assays		
Human R-Spondin-3 Picokine ELISA Kit	Boster Bio	Cat# EK1512
QIAmp DNA Stool Mini Kit	Qiagen	Cat# 51604
Rneasy Mini Kit	Qiagen	Cat# 74104
RT^2 Profiler PCR Array	Qiagen	Cat# 009669
Deposited data		
Bulk RNAseq data of PGE2-treated HDLEC	This paper	GEO: GSE223854
Experimental models: organisms/strains		
Cell line: HDLEC (from juvenile foreskin)	Promocell	Cat# C-12216
Mouse: HdcCre	The Jackson Laboratory	Cat# 021198
Mouse: HdcCreERT2	Chen et al,[37] 2017	
Mouse: HdcGFP	Yang et al,[38] 2011	
Mouse: Ptgs2fl/fl	Gift from Harvey Herschman, University of California Los Angeles	
Mouse: Rosa26-DTA	The Jackson Laboratory	Cat# 009669
Software and algorithms		
clusterProfiler	Wu et al,[70] 2021	https://doi.org/10.18129/B9.bioc.clusterProfiler
FlowJo V10.8	FlowJo, BD	https://www.flowjo.com
GraphPad Prism 9	GraphPad Software	http://graphpad.com
ImageJ version 2.3/FIJI	Schindelin et al[71], 2012	http://imagej.net
QuPath V0.4	Bankhead et al,[66] 2017	http://qupath.github.io

CCR3, C-C motif chemokine receptor 3; DAB, 3,3'-Diaminobenzidine; DAPI, 4′,6-diamidino-2-phenylindole; DPBS, Dulbecco's Phosphate-Buffered Saline; DTT, dithiothreitol; EGF, epidermal growth factor; ELISA, enzyme-linked immunosorbent assay; Ep-CAM, epithelial cellular adhesion molecule; MEK1/2i, mitogen-activated kinase kinase 1/2; PE, phycoerythrin; Ptgs2fl/fl, prostaglandin-endoperoxidase synthase 2 flox/flox; Rspo, R-spondin; SDS, sodium dodecyl sulfate.

RNA template and molecular biology grade water (46-000-CV; Corning). cDNA was synthesized using the following PCR program: 5 minutes at 25°C, 30 minutes at 42°C, and then 5 minutes at 85°C. For all reverse transcriptase quantitative PCR (RT-qPCR) reactions, cDNA was diluted to a final concentration of 5 ng/μL.

Reverse transcriptase qPCR. Reverse transcriptase qPCR was performed by adding equal amounts of cDNA template to a mix of validated gene-specific primers, molecular biology grade water, and PerfeCta SYBR Green FastMix Low ROX (2×) (84073; Quantabio). Real-time qPCR was performed with 3 technical replicates using a QuantStudio3 Real-Time PCR system (Thermo Fisher). Relative expression was calculated as the fold change using the $2^{-\Delta\Delta Ct}$ method. Primer sequences are shown in Tables 1 and 2.

RT^2 Profiler PCR assay. cDNA from isolated Hdc^{GFP} cells was used in the RT^2 Profiler PCR Array (Qiagen) for Mouse Chemokines and Receptors. The manufacturer's protocols were followed.

Bulk RNA sequencing and data processing. Isolated total RNA from HDLECs was measured for purity and integrity (RNA integrity number [RIN], ≥8) on a 2100 Bioanalyzer (Agilent) and then sent to the JP Sulzberger Columbia Genome Center for sequencing. Poly-A pulldown was used to enrich messenger RNAs from samples, and then libraries were constructed using Illumina TruSeq chemistry. RNA sequencing experiments were run on an Illumina NovaSeq 6000 with a sequencing depth of 20 million reads per sample and a targeted number of paired-end 100–base pair reads for each sample. RTA (Illumina) was used for base calling and bcl2fastq2 version 2.19 (Illumina) was used to create FASTQ files and trim adaptors. Pseudoalignment was performed to a kallisto index created from transcriptomes (Ensembl v96, GRGm38.p6) using kallisto version 0.44.0.[72] Differentially expressed genes were determined using DESeq2 version 1.24.0.[73] Gene set enrichment analysis was performed using clusterProfiler version 4.0.[70]

Statistical Analysis

Statistical testing was performed using GraphPad Prism 7 software (GraphPad Software, Inc). For experiments with 2 groups, unless otherwise specified, the differences between the means were compared using the 2-sided Student t test. For experiments with 3 or more groups, 1-way analysis of variance with post hoc Tukey multiple comparisons was performed. For survival experiments, the Kaplan–Meier simple survival analysis was used. Significance was defined as a P value $< .05$.

References

1. Blanpain C, Fuchs E. Stem cell plasticity. Plasticity of epithelial stem cells in tissue regeneration. Science 2014; 344:1242281.
2. McCarthy N, Kraiczy J, Shivdasani RA. Cellular and molecular architecture of the intestinal stem cell niche. Nat Cell Biol 2020;22:1033–1041.
3. Saha S, Aranda E, Hayakawa Y, et al. Macrophage-derived extracellular vesicle-packaged WNTs rescue intestinal stem cells and enhance survival after radiation injury. Nat Commun 2016;7:13096.
4. Antanaviciute A, Kusumbe A, Simmons A. Lymphatic endothelia stakeout cryptic stem cells. Cell Stem Cell 2022;29:1292–1293.
5. Yan KS, Janda CY, Chang J, et al. Non-equivalence of Wnt and R-spondin ligands during Lgr5(+) intestinal stem-cell self-renewal. Nature 2017;545:238–242.
6. McCarthy N, Manieri E, Storm EE, et al. Distinct mesenchymal cell populations generate the essential intestinal BMP signaling gradient. Cell Stem Cell 2020; 26:391–402 e5.
7. Abud HE, Watson N, Heath JK. Growth of intestinal epithelium in organ culture is dependent on EGF signalling. Exp Cell Res 2005;303:252–262.
8. Jarde T, Chan WH, Rossello FJ, et al. Mesenchymal niche-derived neuregulin-1 drives intestinal stem cell proliferation and regeneration of damaged epithelium. Cell Stem Cell 2020;27:646–662 e7.
9. Ogasawara R, Hashimoto D, Kimura S, et al. Intestinal lymphatic endothelial cells produce R-Spondin3. Sci Rep 2018;8:10719.
10. Niec RE, Chu T, Schernthanner M, et al. Lymphatics act as a signaling hub to regulate intestinal stem cell activity. Cell Stem Cell 2022;29:1067–1082 e18.
11. Harnack C, Berger H, Antanaviciute A, et al. R-spondin 3 promotes stem cell recovery and epithelial regeneration in the colon. Nat Commun 2019;10:4368.
12. Choe K, Jang JY, Park I, et al. Intravital imaging of intestinal lacteals unveils lipid drainage through contractility. J Clin Invest 2015;125:4042–4052.
13. Goto N, Goto S, Imada S, et al. Lymphatics and fibroblasts support intestinal stem cells in homeostasis and injury. Cell Stem Cell 2022;29:1246–1261 e6.
14. Palikuqi B, Rispal J, Reyes EA, et al. Lymphangiocrine signals are required for proper intestinal repair after cytotoxic injury. Cell Stem Cell 2022;29:1262–1272 e5.
15. Biswas L, Chen J, De Angelis J, et al. Lymphatic vessels in bone support regeneration after injury. Cell 2023; 186:382–397 e24.
16. Farnsworth RH, Karnezis T, Maciburko SJ, et al. The interplay between lymphatic vessels and chemokines. Front Immunol 2019;10:518.
17. Vaahtomeri K, Brown M, Hauschild R, et al. Locally triggered release of the chemokine CCL21 promotes dendritic cell transmigration across lymphatic endothelia. Cell Rep 2017;19:902–909.
18. Wick N, Haluza D, Gurnhofer E, et al. Lymphatic precollectors contain a novel, specialized subpopulation of podoplanin low, CCL27-expressing lymphatic endothelial cells. Am J Pathol 2008;173:1202–1209.
19. Steele MM, Jaiswal A, Delclaux I, et al. T cell egress via lymphatic vessels is tuned by antigen encounter and limits tumor control. Nat Immunol 2023;24:664–675.
20. Card CM, Yu SS, Swartz MA. Emerging roles of lymphatic endothelium in regulating adaptive immunity. J Clin Invest 2014;124:943–952.
21. Bain CC, Mowat AM. Macrophages in intestinal homeostasis and inflammation. Immunol Rev 2014; 260:102–117.
22. De Schepper S, Verheijden S, Aguilera-Lizarraga J, et al. Self-maintaining gut macrophages are essential for intestinal homeostasis. Cell 2018;175:400–415 e13.
23. Shaw TN, Houston SA, Wemyss K, et al. Tissue-resident macrophages in the intestine are long lived and defined by Tim-4 and CD4 expression. J Exp Med 2018; 215:1507–1518.
24. Smith PD, Smythies LE, Shen R, et al. Intestinal macrophages and response to microbial encroachment. Mucosal Immunol 2011;4:31–42.
25. Kim M, Galan C, Hill AA, et al. Critical role for the microbiota in CX3CR1(+) intestinal mononuclear phagocyte regulation of intestinal T cell responses. Immunity 2018;49:151–163 e5.
26. Muley A, Odaka Y, Lewkowich IP, et al. Myeloid Wnt ligands are required for normal development of dermal lymphatic vasculature. PLoS One 2017;12:e0181549.
27. Machnik A, Neuhofer W, Jantsch J, et al. Macrophages regulate salt-dependent volume and blood pressure by a vascular endothelial growth factor-C-dependent buffering mechanism. Nat Med 2009;15:545–552.
28. Cursiefen C, Chen L, Borges LP, et al. VEGF-A stimulates lymphangiogenesis and hemangiogenesis in inflammatory neovascularization via macrophage recruitment. J Clin Invest 2004;113:1040–1050.
29. Ishikawa TO, Oshima M, Herschman HR. Cox-2 deletion in myeloid and endothelial cells, but not in epithelial cells, exacerbates murine colitis. Carcinogenesis 2011; 32:417–426.
30. He X, Smith SE, Chen S, et al. Tumor-initiating stem cell shapes its microenvironment into an immunosuppressive barrier and pro-tumorigenic niche. Cell Rep 2021;36: 109674.
31. Hull MA, Ko SC, Hawcroft G. Prostaglandin EP receptors: targets for treatment and prevention of colorectal cancer? Mol Cancer Ther 2004;3:1031–1039.
32. Walden TL Jr, Patchen M, Snyder SL. 16,16-Dimethyl prostaglandin E2 increases survival in mice following irradiation. Radiat Res 1987;109:440–448.

33. Tessner TG, Muhale F, Riehl TE, et al. Prostaglandin E2 reduces radiation-induced epithelial apoptosis through a mechanism involving AKT activation and bax translocation. J Clin Invest 2004;114:1676–1685.
34. Roulis M, Kaklamanos A, Schernthanner M, et al. Paracrine orchestration of intestinal tumorigenesis by a mesenchymal niche. Nature 2020;580:524–529.
35. Miyoshi H, VanDussen KL, Malvin NP, et al. Prostaglandin E2 promotes intestinal repair through an adaptive cellular response of the epithelium. EMBO J 2017;36:5–24.
36. Nandi P, Girish GV, Majumder M, et al. PGE2 promotes breast cancer-associated lymphangiogenesis by activation of EP4 receptor on lymphatic endothelial cells. BMC Cancer 2017;17:11.
37. Chen X, Deng H, Churchill MJ, et al. Bone marrow myeloid cells regulate myeloid-biased hematopoietic stem cells via a histamine-dependent feedback loop. Cell Stem Cell 2017;21:747–760 e7.
38. Yang XD, Ai W, Asfaha S, et al. Histamine deficiency promotes inflammation-associated carcinogenesis through reduced myeloid maturation and accumulation of CD11b+Ly6G+ immature myeloid cells. Nat Med 2011;17:87–95.
39. Fu N, Wu F, Jiang Z, et al. Acute intestinal inflammation depletes/recruits histamine-expressing myeloid cells from the bone marrow leading to exhaustion of MB-HSCs. Cell Mol Gastroenterol Hepatol 2021;11:1119–1138.
40. Chen X, Takemoto Y, Deng H, et al. Histidine decarboxylase (HDC)-expressing granulocytic myeloid cells induce and recruit Foxp3(+) regulatory T cells in murine colon cancer. Oncoimmunology 2017;6:e1290034.
41. Booth C, Tudor G, Tudor J, et al. Acute gastrointestinal syndrome in high-dose irradiated mice. Health Phys 2012;103:383–399.
42. Liang L, Shen L, Fu G, et al. Regulation of the regeneration of intestinal stem cells after irradiation. Ann Transl Med 2020;8:1063.
43. Kuramasu A, Saito H, Suzuki S, et al. Mast cell-/basophil-specific transcriptional regulation of human L-histidine decarboxylase gene by CpG methylation in the promoter region. J Biol Chem 1998;273:31607–31614.
44. Crittenden S, Goepp M, Pollock J, et al. Prostaglandin E2 promotes intestinal inflammation via inhibiting microbiota-dependent regulatory T cells. Sci Adv 2021;7:eabd7954.
45. Ishikawa TO, Herschman HR. Conditional knockout mouse for tissue-specific disruption of the cyclooxygenase-2 (Cox-2) gene. Genesis 2006;44:143–149.
46. Sung HK, Morisada T, Cho CH, et al. Intestinal and peritumoral lymphatic endothelial cells are resistant to radiation-induced apoptosis. Biochem Biophys Res Commun 2006;345:545–551.
47. Truman LA, Bentley KL, Smith EC, et al. ProxTom lymphatic vessel reporter mice reveal Prox1 expression in the adrenal medulla, megakaryocytes, and platelets. Am J Pathol 2012;180:1715–1725.
48. Murtomaki A, Uh MK, Choi YK, et al. Notch1 functions as a negative regulator of lymphatic endothelial cell differentiation in the venous endothelium. Development 2013;140:2365–2376.
49. Podgrabinska S, Braun P, Velasco P, et al. Molecular characterization of lymphatic endothelial cells. Proc Natl Acad Sci U S A 2002;99:16069–16074.
50. Azam SH, Smith M, Somasundaram V, et al. Incorporating pericytes into an endothelial cell bead sprouting assay. J Vis Exp 2018;132:57309.
51. Katoh H, Wang D, Daikoku T, et al. CXCR2-expressing myeloid-derived suppressor cells are essential to promote colitis-associated tumorigenesis. Cancer Cell 2013;24:631–644.
52. Xu J, Zhang C, He Y, et al. Lymphatic endothelial cell-secreted CXCL1 stimulates lymphangiogenesis and metastasis of gastric cancer. Int J Cancer 2012;130:787–797.
53. Nighot M, Al-Sadi R, Guo S, et al. Lipopolysaccharide-induced increase in intestinal epithelial tight permeability is mediated by Toll-like receptor 4/myeloid differentiation primary response 88 (MyD88) activation of myosin light chain kinase expression. Am J Pathol 2017;187:2698–2710.
54. Ghosh SS, Wang J, Yannie PJ, et al. Intestinal barrier dysfunction, LPS translocation, and disease development. J Endocr Soc 2020;4:bvz039.
55. Guo S, Nighot M, Al-Sadi R, et al. Lipopolysaccharide regulation of intestinal tight junction permeability is mediated by TLR4 signal transduction pathway activation of FAK and MyD88. J Immunol 2015;195:4999–5010.
56. Kang S, Lee SP, Kim KE, et al. Toll-like receptor 4 in lymphatic endothelial cells contributes to LPS-induced lymphangiogenesis by chemotactic recruitment of macrophages. Blood 2009;113:2605–2613.
57. Yang C, Yu H, Chen R, et al. CXCL1 stimulates migration and invasion in ER-negative breast cancer cells via activation of the ERK/MMP2/9 signaling axis. Int J Oncol 2019;55:684–696.
58. Raduolovic K, Mak'Anyengo R, Kaya B, et al. Injections of lipopolysaccharide into mice to mimic entrance of microbial-derived products after intestinal barrier breach. J Vis Exp 2018;135:57610.
59. Tirelle P, Breton J, Riou G, et al. Comparison of different modes of antibiotic delivery on gut microbiota depletion efficiency and body composition in mouse. BMC Microbiol 2020;20:340.
60. Rakoff-Nahoum S, Paglino J, Eslami-Varzaneh F, et al. Recognition of commensal microflora by Toll-like receptors is required for intestinal homeostasis. Cell 2004;118:229–241.
61. Green DE, Rubin CT. Consequences of irradiation on bone and marrow phenotypes, and its relation to disruption of hematopoietic precursors. Bone 2014;63:87–94.
62. Prinz C, Zanner R, Gerhard M, et al. The mechanism of histamine secretion from gastric enterochromaffin-like cells. Am J Physiol 1999;277:C845–C855.
63. Lin W, Xu L, Zheng Y, et al. Whole-brain mapping of histaminergic projections in mouse brain. Proc Natl Acad Sci U S A 2023;120:e2216231120.
64. Bezencon C, Furholz A, Raymond F, et al. Murine intestinal cells expressing Trpm5 are mostly brush cells and express markers of neuronal and inflammatory cells. J Comp Neurol 2008;509:514–525.

65. Zecharia AY, Yu X, Gotz T, et al. GABAergic inhibition of histaminergic neurons regulates active waking but not the sleep-wake switch or propofol-induced loss of consciousness. J Neurosci 2012;32:13062–13075.
66. Bankhead P, Loughrey MB, Fernandez JA, et al. QuPath: open source software for digital pathology image analysis. Sci Rep 2017;7:16878.
67. Schindelin J, Arganda-Carreras I, Frise E, et al. Fiji: an open-source platform for biological-image analysis. Nat Methods 2012;9:676–682.
68. Couter CJ, Surana NK. Isolation and flow cytometric characterization of murine small intestinal lymphocytes. J Vis Exp 2016;111:54114.
69. Sato T, Vries RG, Snippert HJ, et al. Single Lgr5 stem cells build crypt-villus structures in vitro without a mesenchymal niche. Nature 2009;459:262–265.
70. Wu T, Hu E, Xu S, et al. clusterProfiler 4.0: a universal enrichment tool for interpreting omics data. Innovation (Camb) 2021;2:100141.
71. Schindelin J, Arganda-Carreras I, Frise E, et al. Fiji: an open-source platform for biological-image analysis. Nature Methods 2012;9:676–682.
72. Bray NL, Pimentel H, Melsted P, et al. Near-optimal probabilistic RNA-seq quantification. Nat Biotechnol 2016;34:525–527.
73. Love MI, Huber W, Anders S. Moderated estimation of fold change and dispersion for RNA-seq data with DESeq2. Genome Biol 2014;15:550.

Received August 3, 2023. Accepted October 18, 2023.

Correspondence
Address correspondence to: Timothy C. Wang, MD, Division of Digestive and Liver Diseases, Columbia University Medical Center, 1130 St. Nicholas Avenue, Room 901, New York, New York 10032. e-mail: tcw21@cumc.columbia.edu.

Acknowledgments
The authors thank Harvey Herschman for the generous gift of the Ptgs2$^{fl/fl}$ mice. The authors thank Leah Zamechek, Jonathan LaBella, and Harry Nagendra for their support of their animal colony. The authors are grateful for the support received by Columbia University shared resources, and would like to thank Sun Dajiang "Kevin" (Molecular Pathology Shared Resource), Michael Kissner (Columbia Stem Cell Initiative Flow Cytometry Core Facility), and Erin Bush (Genomics and High Throughput Screening) for their expertise and help during this project. The authors also would like to thank Viki Fernandez for help with manuscript revisions.

CRediT Authorship Contributions
Zhengyu Jiang (Conceptualization: Equal; Investigation: Equal; Methodology: Equal; Writing – original draft: Equal; Writing – review & editing: Equal)
Quin T Waterbury (Conceptualization: Equal; Investigation: Equal; Methodology: Equal; Writing – original draft: Equal; Writing – review & editing: Equal)
Ermanno Malagola (Methodology: Supporting; Writing – review & editing: Supporting)
Na Fu (Investigation: Supporting)
Woosook Kim (Investigation: Supporting; Methodology: Supporting)
Yosuke Ochiai (Investigation: Supporting)
Feijing Wu (Investigation: Supporting)
Chandan Guha (Methodology: Supporting; Writing – review & editing: Supporting)
Carrie J Shawber (Methodology: Supporting; Writing – review & editing: Supporting)
Kelley S Yan (Methodology: Supporting; Supervision: Supporting; Writing – review & editing: Supporting)
Timothy Cragin Wang, MD (Conceptualization: Supporting; Funding acquisition: Lead; Supervision: Lead; Writing – review & editing: Supporting)

Current address of Z.J.: J&J Innovative Medicine, Johnson & Johnson, Spring House, Pennsylvania.

Conflicts of interest
The authors disclose no conflicts.

Funding
This research was funded in part through the National Institutes of Health/National Cancer Institute Cancer Center support grant P30CA013696 and used the resources of the Herbert Irving Comprehensive Cancer Center Flow Cytometry Shared Resources, Molecular Pathology Shared Resources (MPSR), and Genomics and High-Throughput Screening. This research was supported in part by the Columbia University Digestive and Liver Disease Research Center (CU-DLDRC) grant 1P30DK132710-02. This work was supported by National Institutes of Health/National Cancer Institute grants R01DK48077 and R35CA210088 (T.C.W.); as well as National Cancer Institute Outstanding Investigator Award R35CA197745 (T.C.W). Also supported in part by Columbia University Institute of Human Nutrition training grant T32 DK007647-32 (Q.T.W.).

Data Availability
Bulk RNA sequencing data can be found at GEO: GSE223854. The data have been made public. Requests for methods, resources, and reagents should be directed to Timothy C. Wang. Any additional information required to reanalyze the data reported in this article is available from Timothy C. Wang upon request.